CURVATURE AND TWIST MONITORING USING TAPERED FIBER SENSOR

OON WUI LIAM

MASTER OF ENGINEERING SCIENCE

LEE KONG CHIAN FACULTY OF ENGINEERING AND SCIENCE
UNIVERSITI TUNKU ABDUL RAHMAN
MAY 2021

CURVATURE AND TWIST MONITORING USING TAPERED FIBER SENSOR

By

OON WUI LIAM

A dissertation submitted to the Department of Electrical and Electronics Engineering,
Lee Kong Chian Faculty of Engineering & Science,
Universiti Tunku Abdul Rahman,
in partial fulfillment of the requirements for the degree of
Master of Engineering Science
May 2021

ABSTRACT

CURVATURE AND TWIST MONITORING USING TAPERED FIBER SENSOR

Oon Wui Liam

Structural health monitoring (SHM) is a sensor technology for real-time monitoring and damage detection on civil infrastructure through monitoring parameter of the structural such as curvature, deflections, torsions, and strains. This project presents a study of optical fiber sensing system based on tapered fiber for curvature and twist monitoring which can apply on curvature monitoring of roof truss in building. The low fabrication cost and ease of fabrication advantages of tapered fiber make it popular among researchers, but the lack of mature multiplexing scheme for intensity modulated sensor has reduced the practical values of tapered fiber sensor. In this project, two different designs of taper based optical sensor were used in multiplexed curvature sensing and twist sensing. The purposes are to determine the feasibility of tapered fiber sensor in real field test, design a multiplexing sensing array for tapered fiber sensor and design a novel fiber sensor with built-in multiplexer using tapered fiber.

In the first part of the project, two taper based in-line Mach-Zehnder Interferometer (MZI) optical sensors were subjected to curvature sensing on cold-formed steel (CFS) roof truss. Both sensors were attached to CFS roof trusses with the same dimensions of 0.481m × 2.891m × 0.2m with different structural designs. The trusses were subjected to different load tests to determine the performance of MZI sensor under different circumstances. In the first cyclic load test, the MZI sensor achieved ±5% of deviation compared to the commercial LVDT sensor in the repeatability test. Whereas in the failure load test, the MZI sensor is ±3% deviation from LVDT sensor and it was able to discriminate the bending direction change when the truss was loaded to failure.

To improve the practical value of the study, a simple and direct sensing array was demonstrated to operate multiple MZI sensors simultaneously. A parallel topology consisting of two MZI sensors was attached to a hardened steel bar and subjected to curvature measurement. Both sensors shared the same optical source but different optical detectors at the output. A real time monitoring on both MZI sensors was demonstrated and achieved sensitivities of 25.095 dB/km and 29.1 dB/km respectively. The mapping of pristine to multiplexed sensor signal shows a regression coefficient, r^2 of 96.06%, which indicates that the multiplexing setup does not compromise on the sensitivity of the curvature sensor.

In the second tapered sensor design, two loop-integrated tapered fiber (LITF) sensors were fabricated and subjected to multiplexed twist measurement. The LITF sensors have the capability to conduct twist sensing and sub-carrier multiplexing simultaneously through the micro-bending sensitive taper. When subjected to torsion, the output optical power changes linearly with the twist angle. The power modulated signals from both sensors were modulated with a 300 Hz and 250 Hz sub-carrier frequency respectively using acoustic source to discriminate the signals through an overlapping spectrum. Both LITF sensors achieved sensitivities of 0.1634 dB/° and 0.1457 dB/° respectively in the twist measurement. The multiplexing sensing of two LITF sensors using sub-carrier multiplexing (SCM) was demonstrated. To determine the influence of the SCM system to the sensing, a comparison study between pristine and multiplexed setup was conducted. Extinction ratio of the pristine signal is 31.7 dB and multiplexed signal is 25.9 dB, where the attenuation of signal due to SCM system is less than 20%.

ACKNOWLEDGEMENTS

I would like to express my deep gratitude to my supervisor, Dr Lin Horng Sheng and my co-supervisor, Dr Pua Chang Hong. They have given plenty of useful comments, constructive suggestion and clear guidance through the learning process of my master's degree.

This material is based upon work performed at University Tunku Abdul Rahman for Center of Photonics and Advance Materials and supported by Grant UTARRF/2017-C1/L15.

APPROVAL SHEET

This dissertation entitled "**CURVATURE AND TWIST MONITORING USING TAPERED FIBER SENSOR"** was prepared by OON WUI LIAM and submitted as partial fulfillment of the requirements for the degree of Master of Engineering Science at Universiti Tunku Abdul Rahman.

Approved by:

____
(Lin Horng Sheng) Date:…………………….
Assistant Professor/Supervisor
Department of Electrical and Electronics Engineering
Lee Kong Chian Faculty of Engineering & Science
Universiti Tunku Abdul Rahman

____
(Pua Chang Hong) Date: 27/05/2021
Associate Professor/Co-supervisor
Department of Electrical and Electronics Engineering
Lee Kong Chian Faculty of Engineering & Science
Universiti Tunku Abdul Rahman

LEE KONG CHIAN FACULTY OF ENGINEERING AND SCIENCE

UNIVERSITI TUNKU ABDUL RAHMAN

Date: 24 May 2021

SUBMISSION OF FINAL YEAR PROJECT /DISSERTATION/THESIS

It is hereby certified that ***Oon Wui Liam*** (ID No: ***1706801***) has completed this dissertation entitled "*Curvature and Twist Monitoring Using Tapered Fiber Sensor*" under the supervision of Dr. Lin Horng Sheng (Supervisor) from the Department of Electrical and Electronic Engineering, Lee Kong Chian Faculty of Engineering and Science , and Dr. Pua Chang Hong (Co-Supervisor) from the Department of Electrical and Electronic Engineering, Lee Kong Chian Faculty of Engineering and Science.

I understand that University will upload softcopy of my dissertation in pdf format into UTAR Institutional Repository, which may be made accessible to UTAR community and public.

Yours truly,

(*Oon Wui Liam*)

DECLARATION

I hereby declare that the dissertation is based on my original work except for quotations and citations which have been duly acknowledged. I also declare that it has not been previously or concurrently submitted for any other degree at UTAR or other institutions.

Name OON WUI LIAM

Date 24 May 2021

LIST OF TABLES

LIST OF FIGURES

LIST OF ABVREVIATIONS

AOM	Acousto-optic modulator
CFS	Cold-formed steel
EOM	Electro-optics modulator
FBG	Fiber Bragg grating
FPI	Fabry-Perot Interferometer
FSR	Free spectral range
IMD	Intermodulation distortion
LITF	Loop-integrated tapered fiber
LVDT	Linear variable displacement transducer
MI	Michelson Interferometer
MZI	Mach-Zehnder Interferometer
OCT	Optical current transformer
OLTS	Optical loss test sets
OSA	Optical spectrum analyzer

RI	Refractive index
SCM	Sub-carrier multiplexing
SDM	Spatial Division Multiplexing
SHM	Structural health monitoring
TDM	Time Division Multiplexing
WDM	Wavelength Division Multiplexing

TABLE OF CONTENTS

CHAPTER 1

INTRODUCTION

1.1 Background

Global infrastructure crisis is a dilemma where the civil infrastructure suffers from degradation due to aging, neglect and deterioration. For example, the rooftop of a Malaysia's stadium collapsed in 2009, which caused 5 injuries and RM35 million was spent on repair works. European countries such as France, Italy and Germany all face risks of bridge failures. Japan suffered from a serious tunnel failure, where the Sasago Tunnel built in 1977 collapsed in 2012, resulting in 2 injuries and 9 deaths. Aging problem of nuclear power plant is also a concern as more than 70% of the nuclear power plants on Earth are more than 20 years old (Fahad and Chauhdry, 2016; Wallis, 2012; Kim et al, 2018). Therefore, proper inspection systems are needed to monitor the health of infrastructure.

Structural health monitoring (SHM) is a sensor technology by implementing detector on civil structures to monitor the structure's health condition during the service life and detect any damage due to aging, weather and degradation. It is very useful in improving the safety and reliability of a large-scale structure by locating the region that is getting damaged, performing early detection of structure deformation and estimating remaining lifetime of the structure through numerical modelling (Sohn et al, 2002). By finding out and repairing the damage before it spreads, further degradation can be avoided. Thus, reducing the repair costs and avoiding replacement due to catastrophic failure. Failure of inspection and maintenance might eventually lead to casualties and significant property damage.

The applications of SHM using optical fiber sensor are very common in the civil structures. The characteristics of low fabrication cost, ease of fabrication, high sensitivity, compact in size, immunity to electromagnetic interference and resistance to chemical corrosion, give optical sensors significant advantages compared to conventional electrical based sensors.

1.2 Problem Statements

An application of in-line MZI sensor embedded in concrete beam has been conducted for curvature sensing and crack monitoring (Png et al, 2018). The feasibility of tapered based MZI sensor in SHM was experimentally verified. However, due to the low tensile strength characteristic of concrete material, repeatability test is not possible on concrete beam. Thus, there is a need to determine the feasibility and repeatability sensing of MZI sensor on other more elastic materials such as cold-formed steel (CFS).

Besides repeatability test, the capability of multiplexing several MZI sensors on a large civil structure is also considered. Currently, most multiplexing schemes for fiber sensor are not suitable for tapered based MZI sensor which is based on intensity modulation. MZI sensor is a transmissive type intensity modulated sensor. The existing schemes for tapered sensor are usually reflective types using wavelength division multiplexing (WDM) or time division multiplexing (TDM). Both methods are not suitable because MZIs intensity modulated signal is indistinguishable in series topology without encoding the signal with time delay or wavelength (Ji et al, 2012; Jarzebinska,2012; Giraldi et al, 2015). Therefore, a simple and cost-effective multiplexing method is needed to operate multiple MZI sensors.

Other than sensing, tapered fiber also can be used as a multiplexer. A study on using sub-carrier modulation to encode and distinguish the intensity modulated signal through overlapping spectra was published (Roslina et al, 2019). In the study, a sub-carrier signal was generated through periodic modulation of the light intensity, where a single frequency signal is modulated into multiple frequency signals. One of the highlights of the configuration is the entire setup is made up of only optical components. However, the setup of the sub-carrier generator through manipulation of the optical fiber delay length is very complicated and time consuming. To improve the practical value of this project, a simple and cost-effective method is needed to replace the optical based sub-carrier generator.

1.3 Aims and Objectives

The aim of the project is to use tapered fiber to build an intensity based optical sensing system and apply it in SHM. The characteristics of fiber sensor such as high sensitivity, good adaptability to harsh measurement environment, compact, and multiplexing capability are well considered when designing the sensor.

Based on the problems stated above, a few objectives are listed out in this project to overcome the problems:

1. To characterize the repeatability and sensitivity of Mach-Zehnder Interferometer (MZI) sensor on a cold-formed steel (CFS) roof truss.
2. To develop a multiplexed sensing array to operate multiple MZI sensors simultaneously.
3. To design and develop a compact optical sensor with a built-in multiplexer through sub-carrier modulation.

1.4 Thesis Outline

The details of all five chapters in this project are summarized as follows:

- Chapter 1 introduces on the background of this project including SHM, optical fiber sensor, problem statements and the aims & objectives of this project.
- Chapter 2 reviews different types of modulation technique use in optical sensor, applications of optical sensor, multiplexing schemes for intensity interrogation system and working principle of tapered fiber sensor.
- Chapter 3 focuses on the methodology of this project and is further split into three sections. The first section is about SHM on CFS roof truss, second section is on multipoint sensing and the third section is on twist monitoring using a tapered fiber sensor with built-in multiplexer. All sections included sensor fabrication, apparatus setup, experiment procedures and data collecting.

- Chapter 4 comprises the results and discussions of all three experiments including sensor characterization, determine the attenuation due to multiplexing, simultaneous sensing, and the sensing results.
- Chapter 5 concludes all the works in this project and discusses on the possible future works.

CHAPTER 2

LITERATURE REVIEW

2.1 Modulation Techniques of Optical Fiber Sensor

Optical fiber sensor has been widely applied in various fields such as civil structures, transportation structures and renewable energy structures (Lopez-Higuera et al, 2011). The characteristics of low fabrication cost, ease of fabrication, high sensitivity, compact in size, immunity to electromagnetic interference and resistance to chemical corrosion, giving optical sensor a strong competitive edge against the conventional electrical based sensors such as strain gauge and accelerometer. The simplicity of the fiber sensor allows distributed sensing system on a large-scale structure at a relatively low cost. Optical fiber sensors are classified according to the sensor modulation technique and can be separated into four categories: wavelength modulation, phase modulation, polarization modulation and intensity modulation (Nurulain et al, 2017).

2.1.1 Wavelength Modulated Fiber Sensor

Wavelength modulated sensor operates based on the shifting in wavelength corresponding to the sensing parameter. There are a few types of sensor work based on wavelength modulation such as blackbody sensor and fiber Bragg grating (FBG) sensor.

A general blackbody sensor is illustrated in Figure 2.1 (Fidanboylu and Efendioglu, 2009). A metallic coating is coated at one end of the fiber tip forming an isothermal cavity. When the sensing tip is heated, the cavity will glow and act as a light source. The emission of the cavity is approximately equal to the spectral emissive power of a blackbody. The other end of the fiber is connected to detector, where the temperature reading can be obtained from the spectral intensity at two wavelengths.

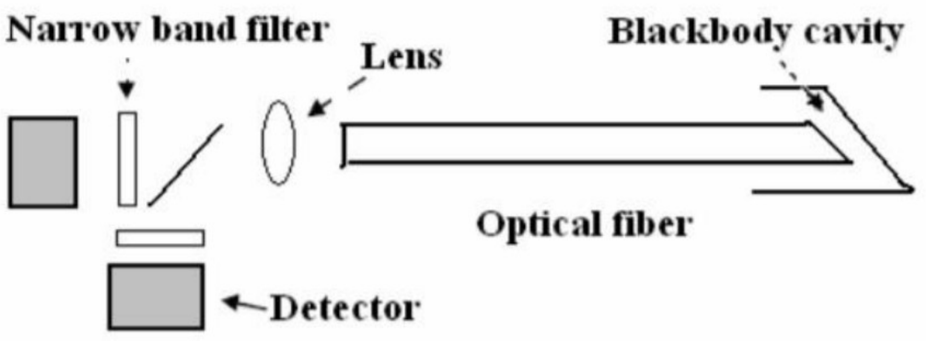

Figure 2.1: Schematic illustration of a typical blackbody fiber sensor. (Fidanboylu and Efendioglu, 2009)

FBG fiber sensor is the most widely used optical fiber sensor in many fields due to its duplicability in fabrication and mature multiplexing scheme. FBG is an intrinsic sensor where a permanent change in refractive index (RI) is created in the fiber core by etching a periodic pattern to the core using UV light. The grating structure with period Λ will induce index modulation to the core, causing the forward propagating core mode to couple with the backward propagating core mode at Bragg wavelength λ_B, which is given by expression (Morey et al, 1989):

$$\lambda_B = 2n_0\Lambda \tag{1}$$

Where n_o is the RI of core.

Figure 2.2 shows the working principle of a typical FBG fiber sensor (Kersey et al, 1997). The grating period, Λ of the FBG will change due to any stretch or expansion on the fiber. When the measurand (e.g. strain and temperature) is changing, the perturbation in grating will result in a shift in the wavelength, λ_B. By monitoring either reflected or transmitted spectrum, the change in measurand will be calibrated to the wavelength shift (Morey et al, 1989).

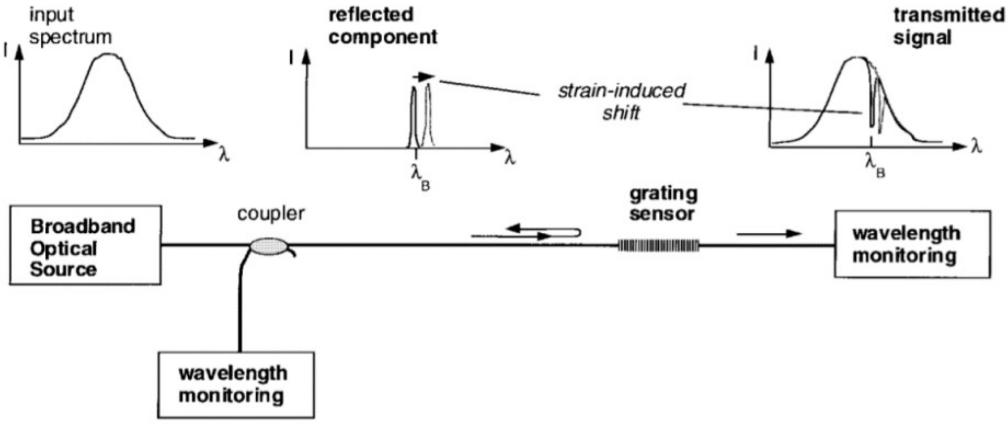

Figure 2.2: Typical FBG fiber sensor setup with reflective and transmissive signal monitoring. (Kersey et al, 1997)

2.1.2 Phase Modulated Fiber Sensor

Phase modulated fiber sensor is also known as interferometric sensor. The phase of the optical signal is modulated in response to the measurand change in the sensing arm, by comparing the phase-shifted signal to the original signal isolated in the reference arm, the phase modulation can be detected. The elongation of the fiber due to stretching or heating will change the optical travel path of the light, thus creating a phase difference between light in sensing arm and referencing arm. Some common types of phase modulated sensor include Fabry-Perot interferometer (FPI), Michelson interferometer (MI) and Mach-Zehnder interferometer (MZI) sensor.

FPI fiber sensor consists of an optical cavity that acts as the sensing component. It can be further classified into intrinsic and extrinsic depend on the configuration of the cavity. The illustrations of intrinsic and extrinsic FPI fiber sensors are shown in Figure 2.3 (Fidanboylu and Efendioglu, 2009). When the incident beam travel across the cavity, the light will experience a reflection from both fiber surfaces. The total reflected optical power from the cavity can be expressed by (Islam et al, 2014):

$$P_r = P_i\left(R_1 + R_2 - 2\sqrt{R_1 R_2}\cos\varphi\right) \tag{2}$$

Where P_i is the incident optical power, R_1 and R_2 are the reflections from each reflective surface, φ is the phase shift from one surface to another. φ can be expressed as:

$$\varphi = \frac{4\pi nL}{\lambda} \tag{3}$$

Where L is the cavity length, n is the RI, and λ is the incident light wavelength. As shown by equation (3), the phase shift of the light is directly proportional to the cavity length. When the FPI sensor is subjected to measurand (e.g. strain, temperature and acoustic), the physical perturbation to the cavity will modulate the light with a phase shift.

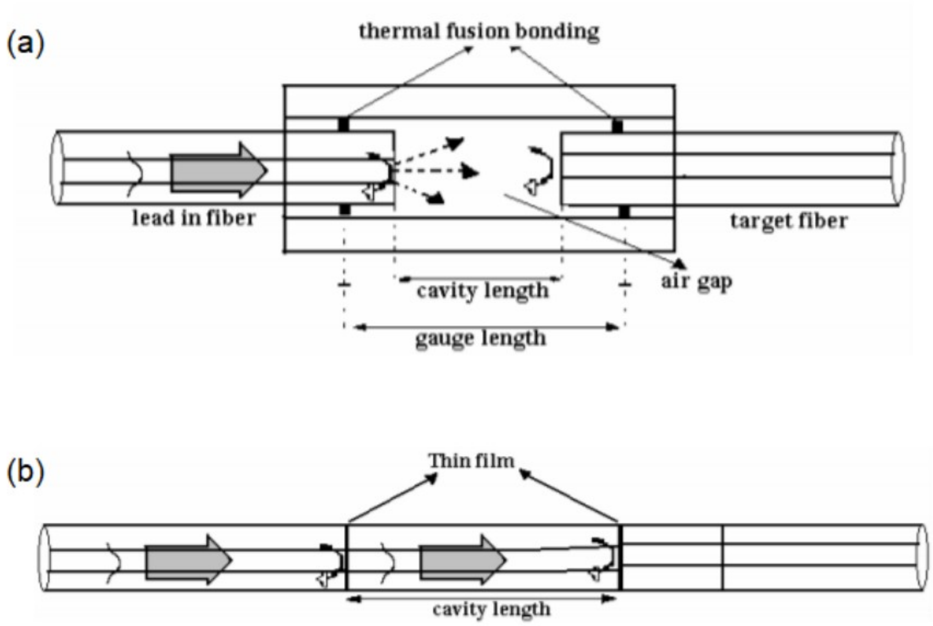

Figure 2.3: Schematic illustrations of (a) extrinsic and (b) intrinsic FPI fiber sensors. (Fidanboylu and Efendioglu, 2009)

MZI fiber sensor also can be classified into two types: two arms structure and in-line structure. The two arms structure consists of two independent arms, which are sensing arm and referencing arm. The configuration of two arms structure MZI is shown in Figure 2.4. An incident light is split into two arms by the first coupler into referencing arm and sensing arm respectively. Later, the light is recombined through the second coupler to form an interference pattern at the output. When the sensing arm is subjected to measurement such as RI sensing (Yuan et al, 2015) and temperature sensing (Zhang et al, 2018), a phase difference $\Delta\phi$ between two arms will occur. In-line MZI fiber sensor is more compact in size because two couplers are integrated on a fiber. The light in the core is coupled into cladding to form reference arm and sensing arm. Both arms have the same physical length but different optical paths due to the modal dispersion, where the cladding has a lower RI than the core. There are plenty of ways to fabricate an in-line MZI. Several of the most common configurations of in-line MZI fiber are LPG pair (Lim et al, 2004), core offset (Rong et al, 2012; Yao et al, 2014), and tapering (Li et al, 2011; Lin et al, 2016; Raji et al, 2016; Png et al, 2018).

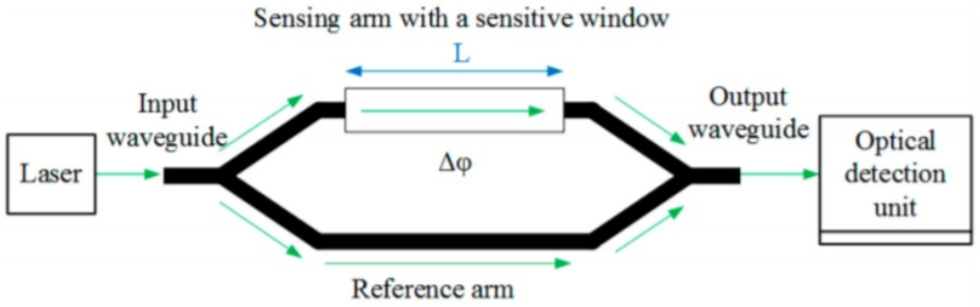

Figure 2.4: Schematic illustration of two arms MZI fiber sensor. (Yuan et al, 2015)

MI fiber sensor is popular in applications such RI sensing and temperature sensing (Zhou et al, 2014; Fu et al, 2016) due to its compact size and practicality. MI sensor is also applied in liquid level measurement which is a variation to RI sensing (Liang et al, 2015). MI sensor is highly similar with the MZI sensor except there is only one coupler to split and recombine the light. The structure of MI two arms configuration is like a half MZI with two mirrors coated at the ends of the fiber as shown in Figure 2.5(a). The working principle is similar to MZI except it involves reflectors which reflect the optical signal backward (Lee et al, 2012).

The structure of an in-line MI sensor is shown in Figure 2.5(b). A mirror is coated at one end of the fiber, where the light travel in both core and cladding will be reflected. The reflected cladding mode will re-couple back to core via the same coupler. Since the light travels twice through the sensing arm, the phase shift per unit length of the fiber is also doubled. Practically, MI sensor is more sensitive than MZI sensor. But the fabrication of MI fiber is more complicated because a high reflective mirror coating is needed (Tian et al, 2008).

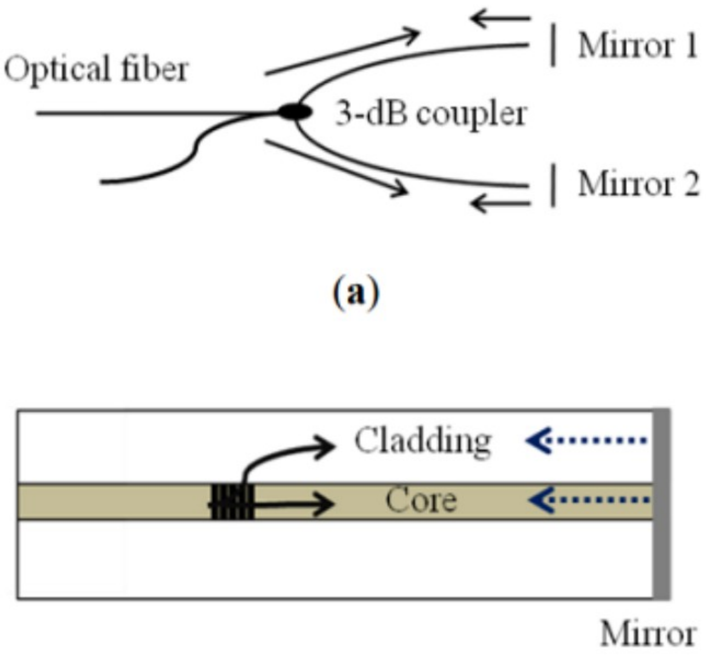

(a)

(b)

Figure 2.5: (a) Two arms configuration of MI sensor. (b) Schematic diagram of in-line MI sensor. (Lee et al, 2012)

2.1.3 Polarization Modulated Fiber Sensor

The operation of a polarization modulated sensor is based on the polarization state change of the light. When a fiber is subjected to stress or strain, the RI of the fiber will change due to the photo-elastic effect. As the incident light enters the polarization modulated sensor, the light will be divided into ordinary ray and extraordinary ray, each propagating at different speeds. The ordinary ray will be governed by the ordinary RI, n_o and the extraordinary ray will be governed by a directional dependent RI, n_e. The relative phase difference $\Delta\phi$ between the ordinary and extraordinary ray can be expressed as:

$$\Delta\Phi = \frac{2\pi}{\lambda} d|n_e - n_o| \tag{4}$$

Where d is the thickness of the birefringent medium.

One example of a polarization modulated sensor is the optical current transformer (OCT). The working principle of OCT is based on the Faraday effect, where the polarization angle of the light is proportional to the external magnetic field. The configuration of an OCT is shown in Figure 2.6. When a linearly polarized incident light travel through a fiber looped around a current, the magnetic field generated by the current flow will induce a rotation to the light at a specific polarization angle. The Faraday rotation angle is given by (Takahashi et al, 1997):

$$\theta = 2VnI \tag{5}$$

Where V is the Verdet constant, n is the loops number and I is the current. A mirror is added at the end of fiber for reflection to remove any perturbation of the differential phase by cancelling out the backward propagating light. The reflected light is then split into two beams to measure their polarization angles respectively. The stronger the electric current flow, the stronger the magnetic field generated, and hence greater angle of rotation (Bohnert et al, 2005).

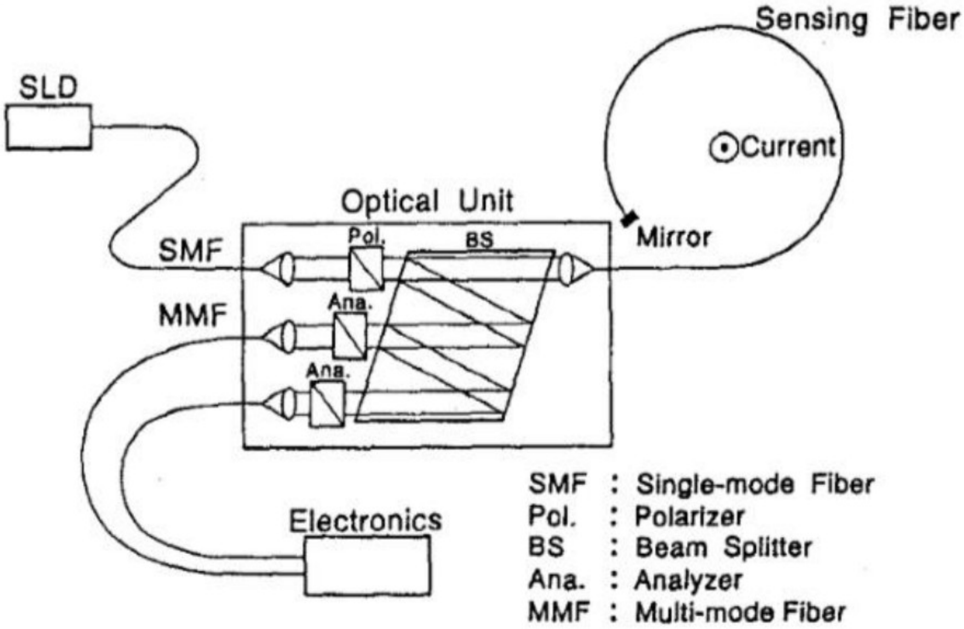

Figure 2.6: Configuration of OCT. A SMF is used as the sensing fiber to detect the magnetic field change of the electric current. (Takahashi et al, 1997)

Another example of polarization modulated sensor is the twist-induced fiber coil sensor. An SMF is looped into a coil as shown in Figure 2.7. A bend-induced fiber coil acts as a retardation plate that creates a phase shift in the transmitted light. The AB_1 and B_2C regions are twist sensitive regions where the circular birefringence occurs. The principle of the sensor is to measure the rotation angle, θ_{coil} of the coil B. During the measurement, the input light of polarization state S_{in} will undergo rotation of θ_{coil} at AB_1 region. Next, the light will enter the coil where phase shift is induced. The phase-shifted light leaves the coil and enter B_2C region, where the light will again rotate at θ_{coil} but in reverse direction, forming an output polarization state of S_{out} (Nathalie et al, 1995).

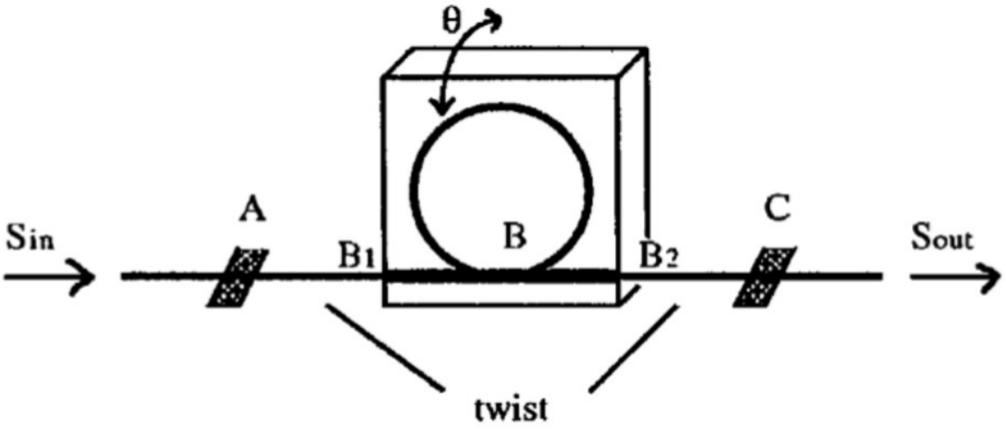

Figure 2.7: Schematic illustration of fiber coil angular displacement sensor. (Nathalie et al, 1995)

2.1.4 Intensity Modulated Sensor

An intensity modulated sensor is based on the optical power loss due to changes in a measuring parameter. When subjected to measurand, the external influences such as bending loss, coupling loss and evanescent field will cause intensity attenuation of the signal. Part of the light will be lost to the surrounding during the measurement and the problem will worsen in multiplex sensing. Therefore, intensity-based sensor usually requires a high energy optical power source. Compared to other types of sensors, the operating cost of intensity-based sensor is relatively low because the sensing only calls for simple instruments such as laser diode and photodetector.

The micro-bend sensor is a displacement sensor. When a force is applied to the sensor as shown in Figure 2.8, the grooved structure of the blocks will squeeze the fiber, causing the fiber to bend. As the pressure increases, the bending radius increases as well. When the bending radius exceeds the critical angle of the total internal reflection to confine the light in the guided mode, the light will be coupled to radiation modes and eventually lost to the surrounding. The attenuation of the power results in intensity modulation of the light (Berthold, 1995; Fidanboylu and Efendioglu, 2009).

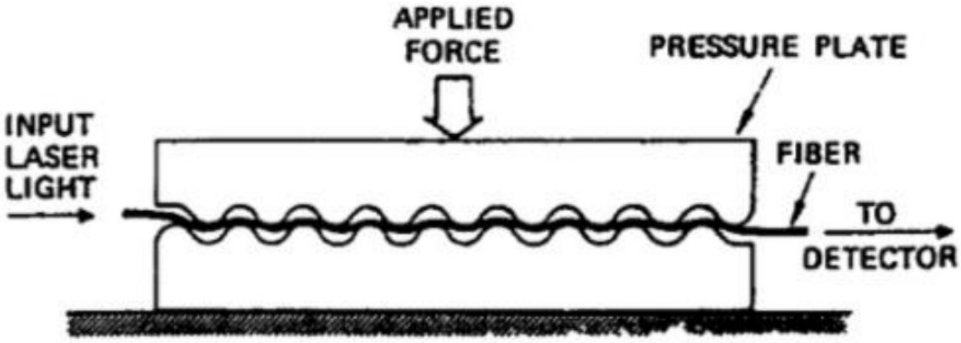

Figure 2.8. Schematic illustration of a micro-bend sensor. (Berthold, 1995)

2.1.5 Intensity Interrogation System

Besides the intensity-based sensor, the intensity interrogation method is also applicable to other modulation sensors. As stated in section 2.1.4, the operation cost of intensity interrogation is relatively lower compared to phase shift, polarization and wavelength interrogation (Cheng and Xia, 2015; Jun et al, 2015; Ibrahim et al, 2016). The conversion into intensity interrogation method is applicable to other three types of sensor.

One of the examples is the edge filter-based interrogation technique. An edge filter was used to induce intensity modulation to the spectrum of FBG sensor. The idea is to achieve wavelength-to-intensity linear conversion for sensing and turn the FBG sensor into an intensity-based sensor. The variation of the intensity at the shifted wavelength due to the edge filter is shown in Figure 2.9 (Deepa et al, 2014).

Another method is by encoding the sensor with a specific wavelength. Figure 2.10 shows a study of using intensity-curvature relation instead of the wavelength shift-curvature relation in the measurement of MZI sensor, where the measurement was done by measuring the FSR spectrum amplitude at a specific wavelength (Raji et al, 2016; Lin et al, 2016).

For polarization modulated sensor, the output state of polarization can be measured by intensity variation through a fixed polarizer at the fiber end as shown in Figure 2.11 (Nathalie et al, 1995).

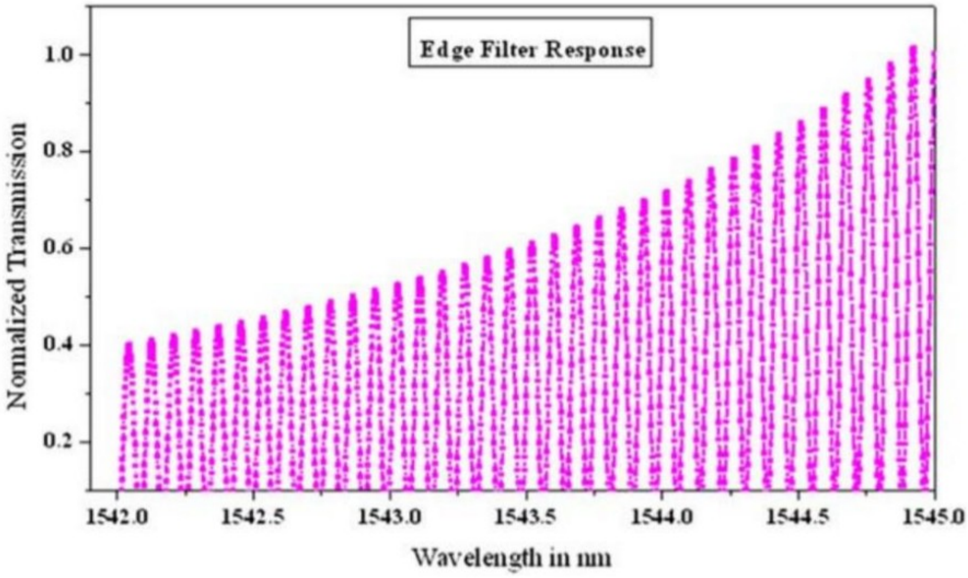

Figure 2.9: Wavelength-to-intensity linear conversion of FBG sensor by using a chirped FBG as edge filter. (Deepa et al, 2014)

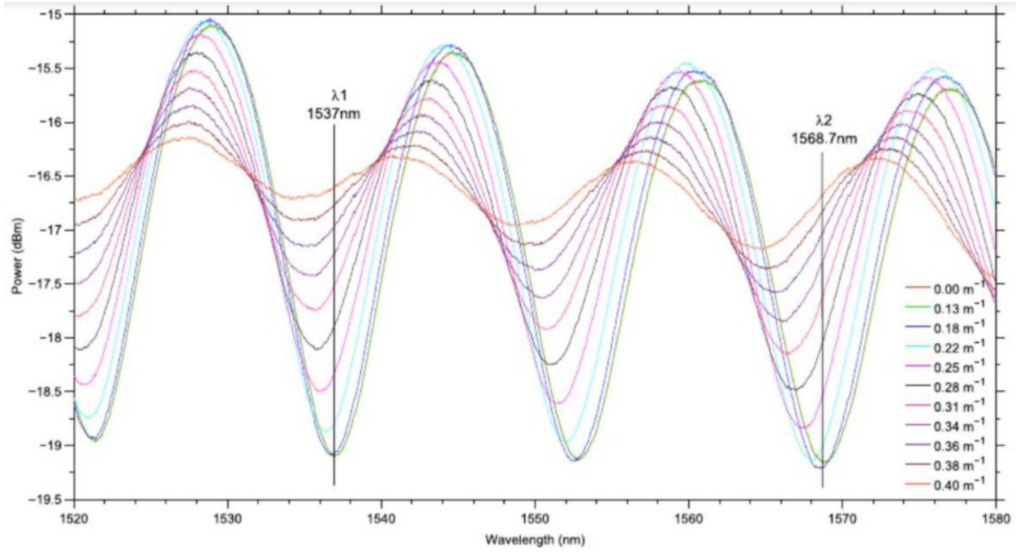

Figure 2.10: Spectrum shift of MZI sensor when applied to curvature sensing. Two intensity readings are taken at wavelength of 1537 nm and 1568.7 nm respectively. (Raji et al, 2016)

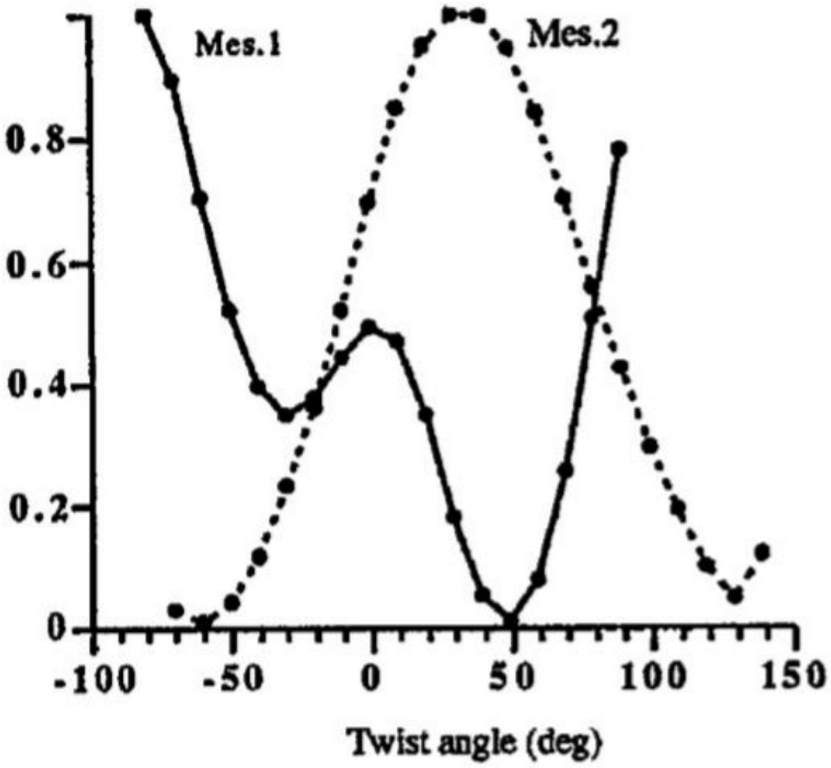

Figure 2.11: The intensity of the polarization-based sensor output versus the twist angle of the polarization modulated fiber. (Nathalie et al, 1995)

2.2 Application of Optical Sensor

2.2.1 Strain Sensing

Strain is one of the most common measurement parameters in SHM to describe deformation, debonding and degradation of the entire structure. FBG sensor is a very mature strain sensing device. It can be used for point sensing or distributed sensing over a structure. The mature wavelength interrogation system allows simultaneous monitoring of multiple points with a simple and compact setup (Kreuzer, 2006). A single fiber can contain more than 20 FBGs and potentially up to 100. The interrogation system assigns each FBG with a specific Bragg wavelength, which is reflected when the incident light passes through the grating. When FBG is subjected to strain, the relative Bragg wavelength shift is expressed as (Majumder et al, 2008):

$$\frac{\Delta\lambda_B}{\lambda_B} = (1 - \rho_e)\varepsilon \tag{6}$$

Where ρ_{ev} is the effective photo-elastic constant of the core and ε is the longitudinal strain.

By detecting and measuring the shift in wavelength of the reflected light, the induced strain on the FBG can be calculated. A schematic diagram of FBG sensor working principle is shown in Figure 2.12 (Krohn, 1988).

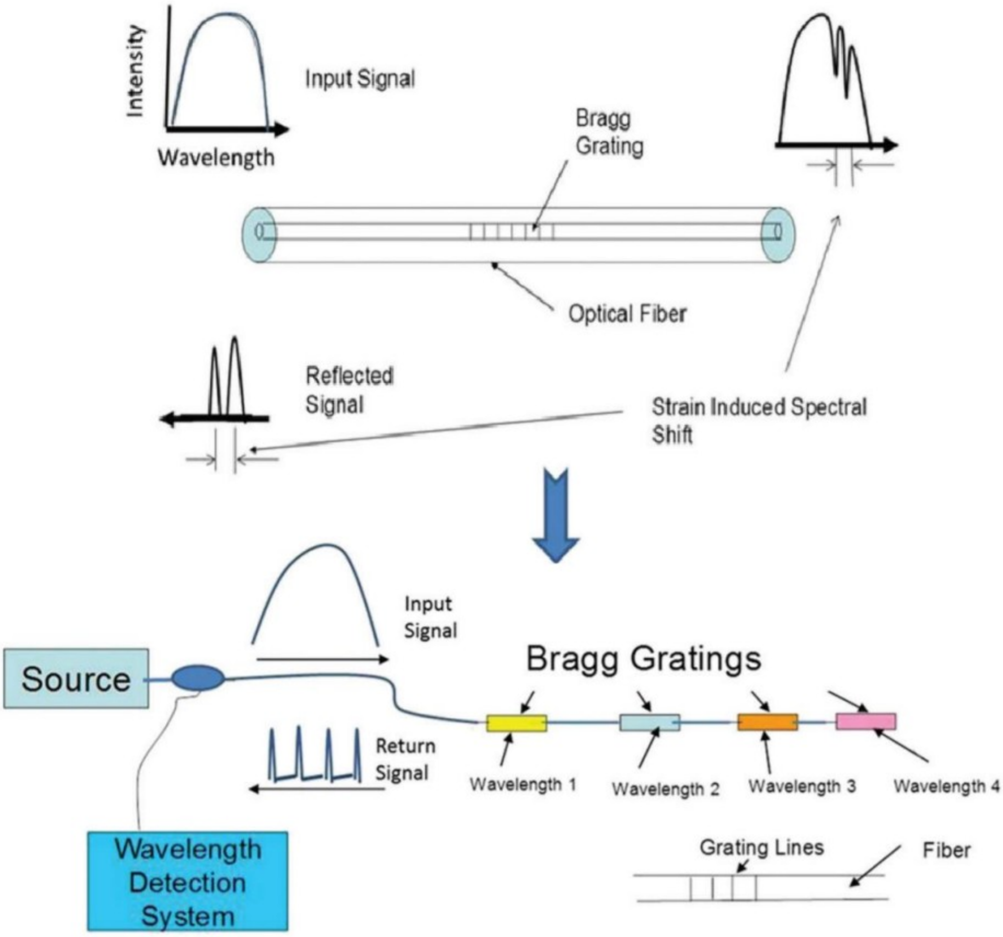

Figure 2.12: Schematic diagram of FBGs sensing system. (Krohn, 1988)

2.2.2 Curvature Sensing

Curvature sensor is usually treated as an alternative to strain sensor. Strain sensing focuses on the monitoring of structure material (e.g. concrete, steel and wood) and observing their behavior under load, temperature change and aging (Inaudi et al, 1998). On the other hand, curvature sensing focuses on the monitoring of the entire structure, it can be performed at any location of the structure without being affected by the structure's thickness (Fernandes et al, 2016).

In the application of curvature sensing, MZI-based curvature sensor with a higher sensitivity for directional discrimination has successfully drawn the attention of researchers over FBG-based sensor. Besides that, MZI-based sensor also has a greater potential of real time monitoring on the structural deformation (Markovic et al, 2015; Lee et al, 2012).

A research of tapered MZI-based sensor embedded in concrete beam for curvature sensing and crack detection has been conducted by Png et al. (2018). In the experiment, a tapered in-line MZI fiber was well packaged between two polypropylene slabs and embedded into a concrete beam. The sensor was attached to a reinforced steel bar before the concrete beam was cast. A load is subjected to the concrete beam at the mid span using four points bending machine as shown in Figure 2.13.

A linear vertical displacement transducer (LVDT) was installed at the middle bottom of the beam to measure the vertical deflection, *d* during the load test. The intensity change of the output is calibrated to the curvature. This experiment has successfully proven the feasibility of applying packaged in-line MZI sensor in SHM. However, due to the concrete's characteristic of low tensile strength, the beam immediately cracked and failed after loading. Thus, the repeatability and directional discrimination of in-line MZI sensor in SHM have yet to be proven.

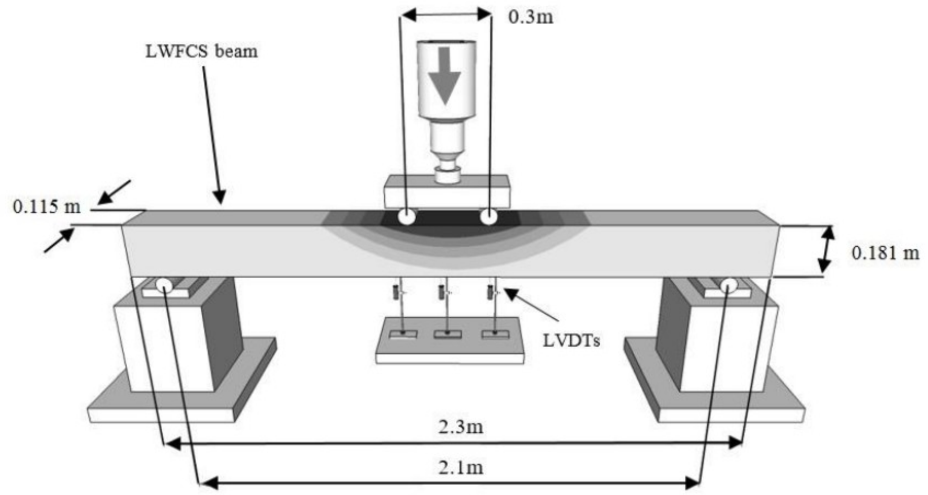

Figure 2.13: Schematic diagram of load test on a concrete beam embedded with MZI sensor. (Png et al., 2018)

2.2.3 Acoustic Sensing

Acoustic sensor is used to measure acoustic emission generated in a material when it is subjected to stress or pressure. The acoustic emission is a sudden release of energy from a local source within the material due to internal structure change. By measuring the acoustic emission, we will be able to determine the internal cracking of the structure.

One of the working principles of optical acoustic sensor is based on phase modulation with interferometric sensor. When exposed to external acoustic vibration, the acoustic pressure-induced RI variation will change the RI of the fiber (Bucaro et al, 1977; Johny et al, 2017). This will change the optical path of the light in fiber and result in change of phase. But due to the limitation of existing technology, the phase change is normally obtained via the measurement of light intensity change. The intensity of the interference light is expressed as:

$$E^2 = E_1 + E_2 + 2E_1E_2 \cos(\Delta\phi + \Delta\phi_0) \qquad (7)$$

Where the E_1 and E_2 are the amplitudes of the light in sensing arm and reference arm respectively, $\Delta\phi_0$ is the initial phase difference between two coherence light and $\Delta\phi$ is the phase difference induced by the acoustic pressure (Li et al, 2011; Wang et al, 2019).

Another vibration sensing scheme is proposed by using tapered fiber. Tapered based acoustic sensor is based on power demodulation due to micro bending loss. It has the advantages of simple setup, does not require a coherent source and insensitive to temperature changes over interferometric sensor. As shown in the Figure 2.14, the bending of the taper will cause a transition of optical power from fundamental (HE_{11}) mode to higher order mode. When a tapered fiber is subjected to vibration, the periodic bending of taper will induce a frequency modulation on the transmitted light based on the vibration frequency (Xu et al, 2012).

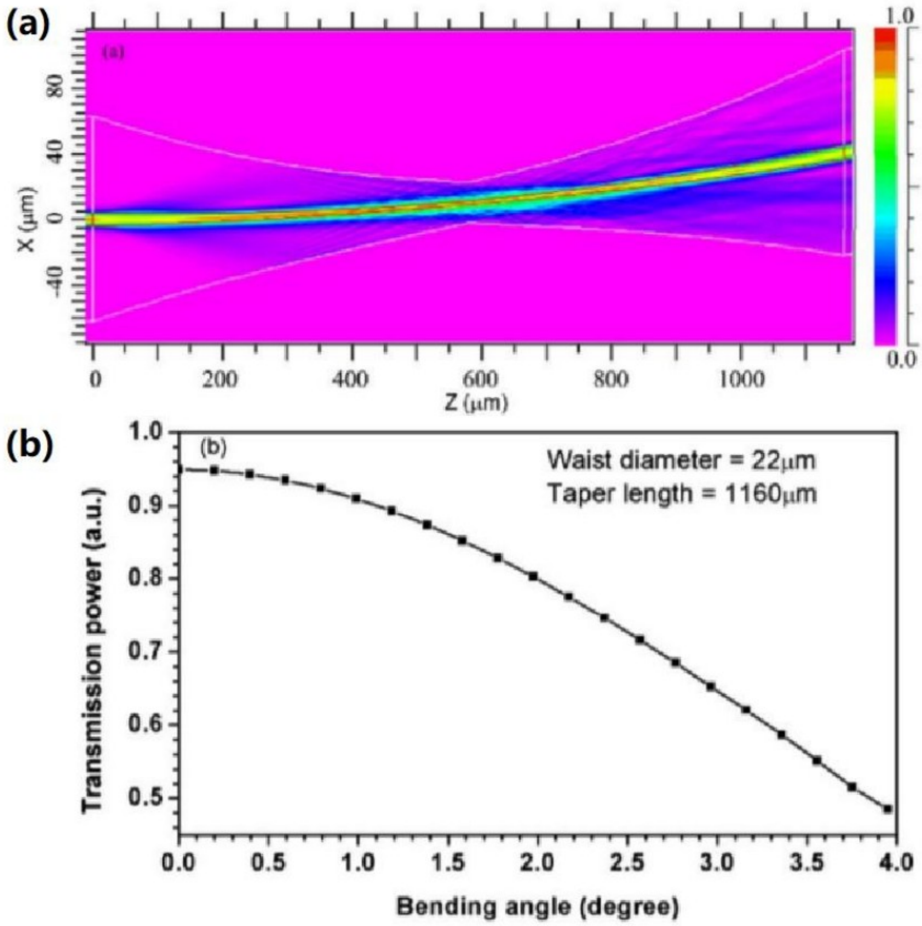

Figure 2.14: (a) A simulation result of the amplitude distribution of abrupt tapered fiber when the taper is bent. (b) The transmission power change corresponding to the taper bending angle. (Xu et al, 2012)

2.3 Multiplexing Schemes for Intensity Interrogation System

As stated in section 2.1.5, intensity interrogation system has the advantages of low operating cost and simplicity of setup. However, to apply the intensity-based sensor into SHM application, a complete operating system that allows multiple points sensing is needed. The wavelength division multiplexing (WDM) often used in wavelength interrogation system is not directly applicable to intensity modulated sensor without addition of extra components such as filter element. Other than WDM, there are a few types of multiplexing methods that are feasible for the intensity modulated sensor.

2.3.1 Time Division Multiplexing

Time division multiplexing (TDM) operates by inducing a time interval between each pulsed signal. It can be accomplished by manipulating the fiber length to create different optical paths and the signals are distinguished based on the arrival times. A TDM sensing array concept is illustrated in Figure 2.15. A pulse of light is sent into the transducer. Upon entering the transducer, the light is split into multiple channels where each channel consists of one or more sensor head. Each channel is encoded with a unique delay line which can be manipulated by adjusting the fiber length. The sensor with the shortest delay line will be the first to receive the pulse signal and reflect it back to the receiver. Since all channels have a unique delay line, the reflected optical signals will be separated by the time of arrival (Dones and Varshneya, 1994).

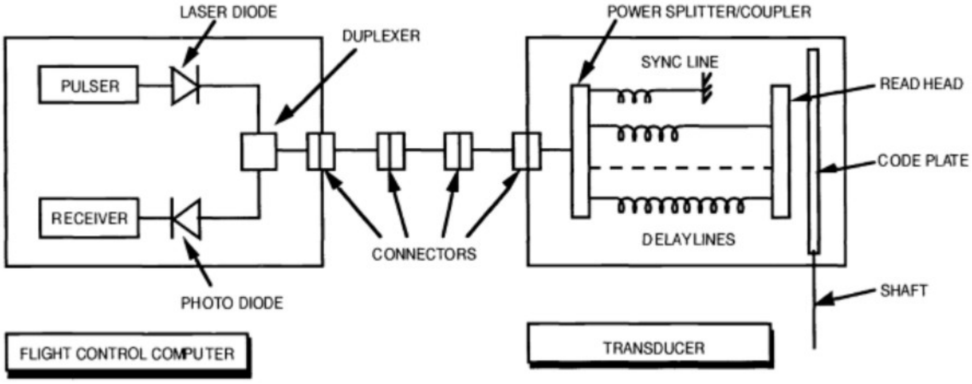

Figure 2.15: Schematic illustration of the TDM sensing array. (Dones Varshneya, 1994)

2.3.2 Spatial Division Multiplexing

Another commonly found multiplexing method is spatial division multiplexing (SDM). The fundamental idea of SDM is to share a single optical light source with all sensors through one or more splitter. It physically increases the number of spatial channels to allow optical signal's transmission via different optical paths (Peng et al, 2004). Depending on the design, SDM sensing system usually will share the same detector as well. All types of SDM topologies for reflective sensor and transmissive sensor are shown in Figure 2.16 (Jason, 2008).

SDM is the most straightforward multiplexing scheme for intensity interrogation system. Figure 2.17(a) shows the configuration of a parallel topology sensor network where a 1×4 coupler is used to split the incident light into four channels, each assigned with one sensor. The isolation of the optical paths helps to avoid optical crosstalk between channels as each sensor in the network has an independent output connected to its respective detector. Thus, the intensity modulated signals of each sensor can be distinguished by monitoring the reading on detectors. Figure 2.17(b) shows an alternative configuration to the topology where an optical switch is replacing the coupler.

A drawback of this method is the reduction of light intensity when it splits into multiple channels. The portion of the light that transmits through each sensor is divided according to the number of channels. Therefore, a high optical power laser source is needed in order to multiplex more sensors.

SDM is often used together with other multiplexing methods. One of the common examples is the combination of SDM and WDM in FBG sensor array. This topology possesses the advantages of both series and parallel topologies, forming a two-dimensional quasi distributed sensor network which can greatly increase the number of FBG in the network (Rao et al, 1996).

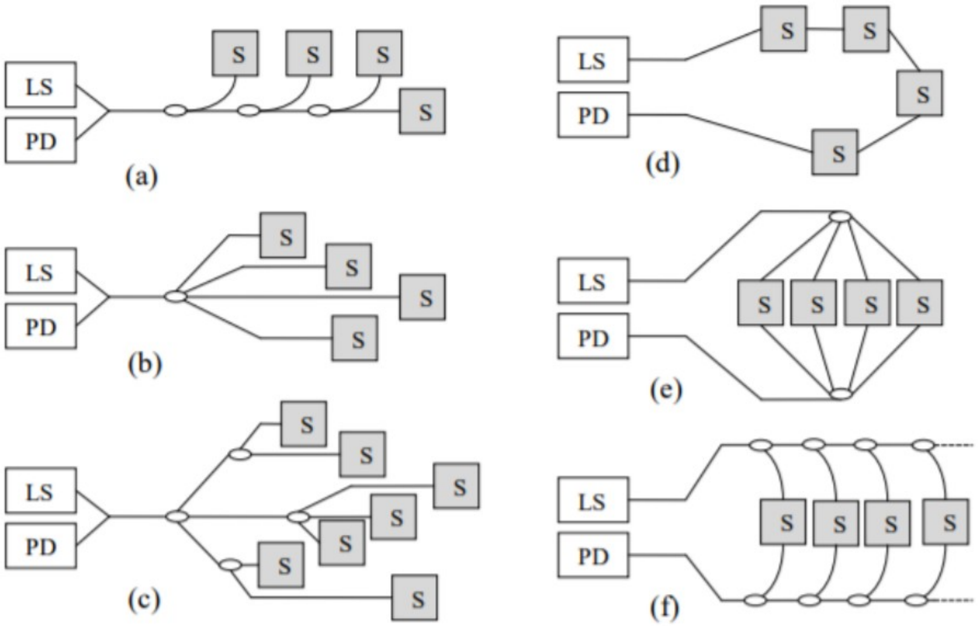

Figure 2.16: Schematic diagrams of point sensor topology for reflective type sensor (a) linear, (b) star, (c) tree, and transmission type sensor (d) ring, (e) star, (f) ladder. (Jason, 2008)

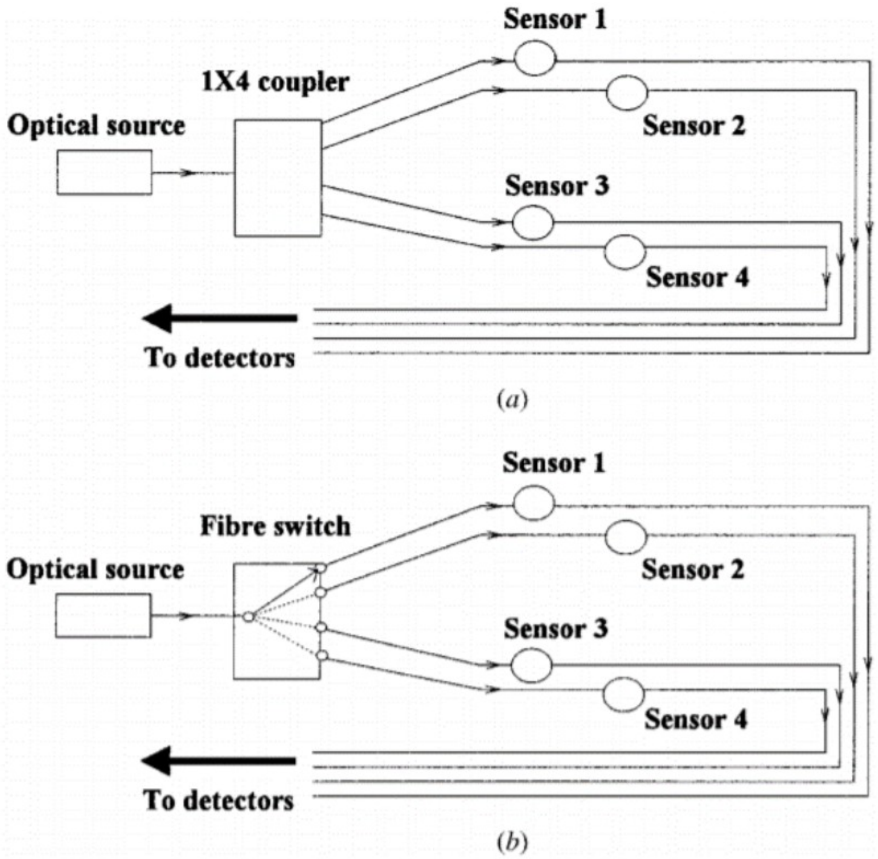

Figure 2.17: Schematic diagrams of SDM sensor array with (a) fixed configuration and (b) switched configuration. (Senior, 1998)

2.3.3 Sub-Carrier Multiplexing

Sub-carrier multiplexing (SCM) for sensing array is achieved by modulating each sensor with a different sub-carrier and combining all the sensor information into single output. Figure 2.18 shows a setup of two LPG sensors in SCM array. The coupled light is modulated by an electro-optic modulator (EOM) in response to the signal generator. Each LPG requires an EOM to modulate its signal with a unique carrier frequency. The individual spectrum response will be demultiplexed through an overlapping spectrum where the signals are distinguished with their respective frequency of carrier (Lin et al, 2009).

A passive SCM experiment conducted by Roslina et al. (2019) reported to have used fiber component to set up the sub-carrier generator as shown in Figure 2.19. The sub-carrier generator is used to generate a new carrier signal from the input carrier through periodic modulation of light intensity. The output waveform is formed by pulse positioning technique where input is split into different channels in parallel and propagated through different optical delay lines. The pulse signals with different time delays will combine with equal pulse spacing to produce an output carrier that is different from the input.

The passive SCM setup requires only one EOM to generate the first carrier signal, which makes the setup more cost effective. However, the setup of the passive sub-carrier generator is very complicated and bulky as the delay line of each parallel channel must be well calculated to obtain the desired frequency output. When the number of sensors in the sensing array increases, the complexity and the bulkiness of the system will also increase substantially.

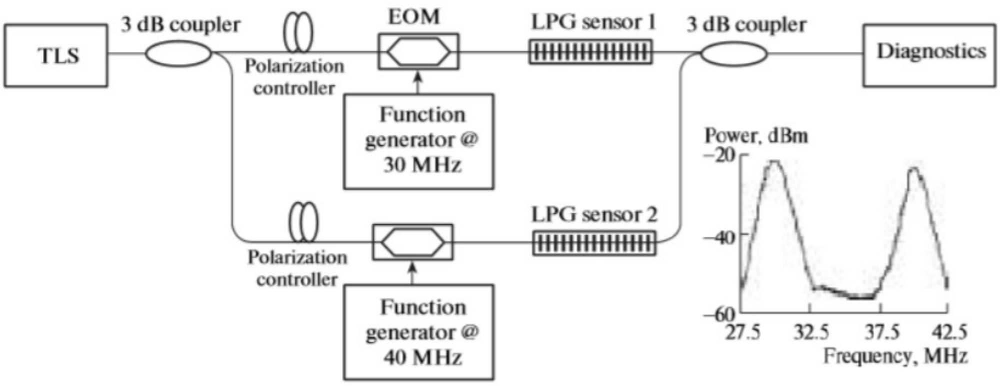

Figure 2.18: Schematic diagram of SCM sensing array for LPG sensors. Two EOM was used to modulate each LPG with respective carrier. (Lin et al, 2009)

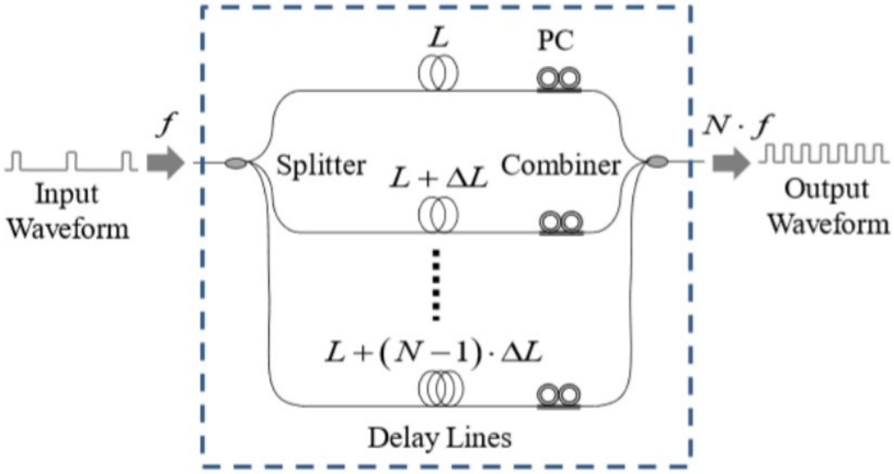

Figure 2.19: Schematic diagram of the optical sub-carrier generator made from fiber component only. (Roslina et al, 2018)

2.4 Tapered Optical Fiber Sensor

Tapering is one of the simplest ways to fabricate optical sensing element. It offers several features that are highly attractive in the sensor development including compactness, ease of fabrication, and large evanescent field. The measurement of tapered sensor is normally done by detecting the light losses within the taper region when the taper is exposed to external parameter such as RI, acoustic vibration and rotation (Korposh et al, 2019).

2.4.1 Comparison of Optical Fiber Sensor and Conventional Sensor on SHM

A robust SHM sensor is only sensitive to the target measurand and insensitive to other external influences. Compared to conventional electrical sensor, optical fiber sensors offer important features that are not available in electrical based sensor, such as immune to electromagnetic interference, capability to operate in high temperature, high sensitivity, multiplexing capability, and compactness.

Table 2.1 shows a list of optical fiber sensor and conventional sensor together with their measured parameter and applications in SHM. FBG fiber sensor is one of the most common commercial optical fiber sensors that can be found on the market. FBG sensors show an outstanding performance in sensitivity, multiplexing capability and miniature size when compared to conventional electrical sensors. Meanwhile, most taper based sensor such as in-line MZI sensor are still in experimental stage. Intensity based tapered fiber sensor provided high performance in sensing and much lower operating cost compared to FBG sensors, but the multiplexing capacity and the sensor durability are not good enough to be commercialize. Further research is needed to improve the practical value of intensity based tapered fiber sensor.

Although the conventional electrical sensor that getting smaller and lighter as the miniature techniques advanced., but fiber sensors are still way more compact in size compared to most of the electrical sensors. The extreme compactness of fiber sensors allows it to be apply to any harsh environments and narrow spaces. One of the advantages of the optical fiber sensor is the simultaneous measurement of multiple measurand using single sensing probe. For example, in-line MZI sensor is capable of carry out temperature and curvature sensing simultaneously with one sensor head. A well packaged in-line MZI sensor is able to measure both physical properties by measuring the wavelength shift and amplitude change on the interference output (Raji et al, 2016). By combining multiple parameters sensing into one sensor probe, the optical fiber sensing system will become more compact.

Table 2.1. Applications of optical fiber sensor and conventional electrical sensor in SHM.

Ref	Parameter	Applications in SHM	Optical Fiber Sensor	Conventional Sensor
Rong et al, 2017; Yao et al, 2016; Guozhen et al, 2016)	Acceleration	Measure the static gravitational force on structure and sense motion or vibration	FBG acceleration sensor	Piezoelectric accelerometer
Raji et al, 2016; Png et al, 2018	Curvature	Detecting structure deformation and monitor the bending of the measurand	In-line MZI sensor	Strain gauge
Metie et al, 2008; Zhu et al, 2017	Displacement	Monitoring the displacement of the existing tunnel or structure when other construction activities occur nearby	Micro-displacement fiber sensor based on surface plasmon resonance	Linear vertical displacement transducer (LVDT)
Sikarwar et al, 2017	Pressure	Detecting pipeline leakage, flow sensing, and crack	Intensity based piezo-optic	Piezoelectric pressure sensor, load

		sensing	pressure sensor	cell
Kreuzer et al, 2006	Strain	Measure the effect of external force on the structure	FBG strain sensor	Strain gauge, vibrating wire traducer
Raji et al, 2016; Lupi et al, 2008	Temperature	Detecting the temperature change on the structure	FBG based thermal sensor, MZI based thermal sensor	Semiconductor based thermal sensor, thermocouples, thermistor
Ong, 2017; Soh, 2018	Vibration	Detecting acoustic vibration causes by the leakage of liquid on pipeline	Looped MZI sensor	Acoustic emission (AE) sensor

2.4.2 Fabrication of Tapered Fiber

The fabrication of the taper is done by applying heat on the SMF-28 fiber integrated with one sided pulling mechanism (Ward et al, 2006; Mukhtar et al, 2010). The waist diameter of the taper is controlled by manipulate the stretching distance. Since the relationship between the waist diameter and sketching distance obeys the law of volume conservation, the volume of fiber before and after stretching can be expressed as:

$$\frac{\pi}{4}(D_o + \delta D_w)^2(L + \delta x) = \frac{\pi}{4}{D_o}^2 L \tag{8}$$

Where D_o is the diameter of the SMF-28 fiber, δD_w is the change in fiber waist diameter, δx is the stretch distance and L is the hot zone of the electric arc.

2.4.3 Working Principle of Tapered Based In-line MZI Sensor

Tapered based in-line MZI sensor consists of two tapers on a SMF, where the tapers will act as couplers to split the light from core into cladding. The schematic diagram of the working principle is shown in the Figure 2.20. The first taper in the MZI fiber allows HE_{11} mode to couple into higher order leaky mode, thus forming two different optical travel paths. After surviving a short period in the cladding, the leaky mode will be re-coupled back into the core at the second taper forming an intermodal interference. The resultant intensity of the interference is given as (Wang et al, 2010):

$$I(\lambda) = I_1(\lambda) + I_2(\lambda) + 2\sqrt{I_1(\lambda)I_2(\lambda)}cos\left[\frac{2\pi \bigtriangleup n_{eff}L}{\lambda}\right] \tag{9}$$

where $I_1(\lambda)$ and $I_2(\lambda)$ are the intensities of light in the core and cladding respectively, Δn_{eff} is the RI difference between the core and cladding, and L is the interferometer length between two tapers.

The free spectral range (FSR) of the interference fringe is given as:

$$FSR = \frac{\lambda^2}{\Delta nL} \tag{10}$$

Where L is the interferometric length between two couplers. Any external perturbation exerted on the MZI sensor such as bending, heating and elongation will create a variation to the interferometric length, ΔL. Thus, the output interference spectrum will shift according to the elongation and it is often applied to the curvature measurement (Lin et al, 2016; Png et al, 2018)

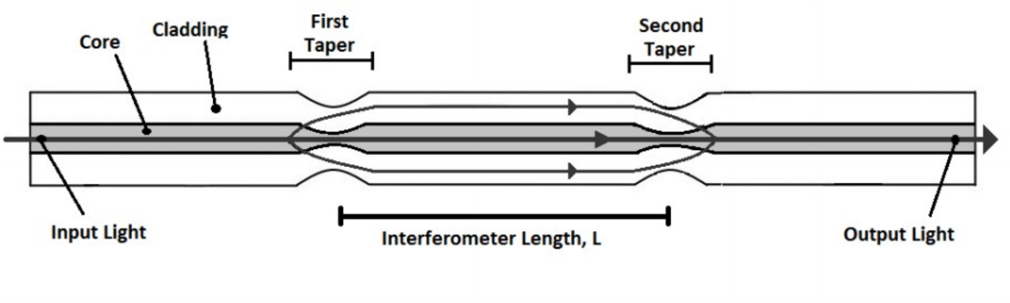

Figure 2.20: Illustration of a tapered in-line MZI fiber sensor.

2.4.4 Tapered Acoustic Vibration Sensor

Tapered acoustic vibration sensor uses a thin tapered fiber as the sensor head to detect acoustic vibrations. The vibrations are detected by direct measurement of the tapered fiber's transmission power. A simple configuration of tapered fiber acoustic sensor is shown in Figure 2.21, where a tapered fiber is mounted on a metal plate to detect the vibration generated by a commercial speaker (Xu et al, 2012). The sensor has a wide frequency sensitive range.

The working principle of the sensor is based on the micro bending of the taper. When subjected to vibration, the change in longitudinal strain of tapered fiber will cause the phase change in the HE_{11} mode. The phase change, $\Delta\varphi$ induced by an elongation ΔL in an SMF is given by (Wild et al, 2008):

$$\Delta\varphi = k(n\Delta L + \Delta n L) \tag{11}$$

Where k is the wave vector, L is the original length of fiber and ΔL is the change in fiber length when subjected to vibration. But the phase change is more complicated in tapered fiber. By taking the tapered fiber profile into consideration, the phase change, $\Delta\varphi$ becomes (Li et al, 2011):

$$\Delta\varphi(z) = k \cdot n(z) \cdot \varepsilon(z) \cdot \left\{1 - \left[\frac{n(z)^2}{2}\right] \cdot [p_{12} - \upsilon(p_{11}p_{12})]\right\} \cdot dz \tag{12}$$

Where n(z) is the n_{eff} along the tapered fiber, $\varepsilon(z)$ is the local strain, p_{11} and p_{12} are the optoelastic constants of the silica. Based on equation (12), the n_{eff} of the HE_{11} mode is calculated and plotted in Figure 2.22. The plot shows that when light propagates in the HE_{11} mode of a tapered fiber, the n_{eff} of the HE_{11} mode will become smaller than the cladding when the taper diameter drops below 50, and the n_{eff} drops rapidly when the diameter approaches 20 µm. This indicates that for acoustic sensing, the smaller the taper diameter, the more sensitive the taper is to the vibration.

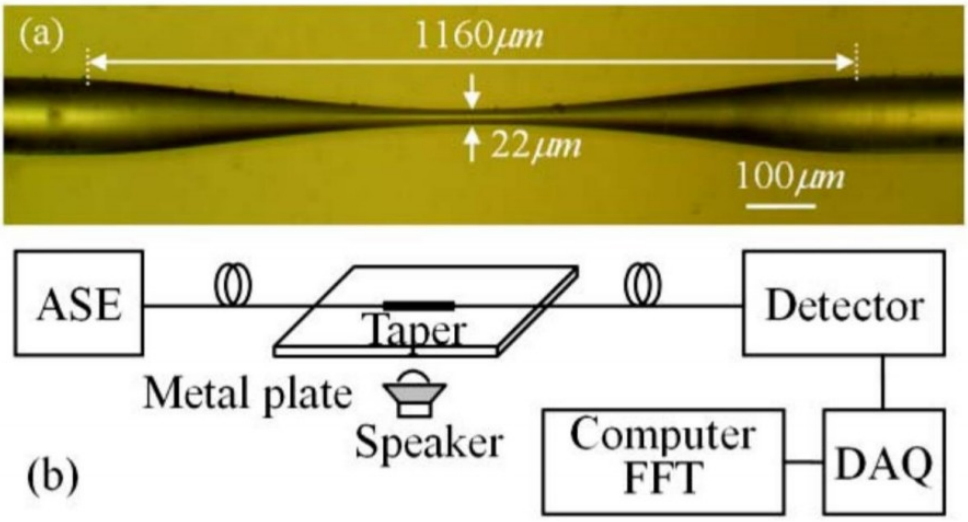

Figure 2.21: (a) A microscopic view of the tapered fiber. (b) The experiment setup of tapered fiber for acoustic vibration sensing (Xu et al, 2012).

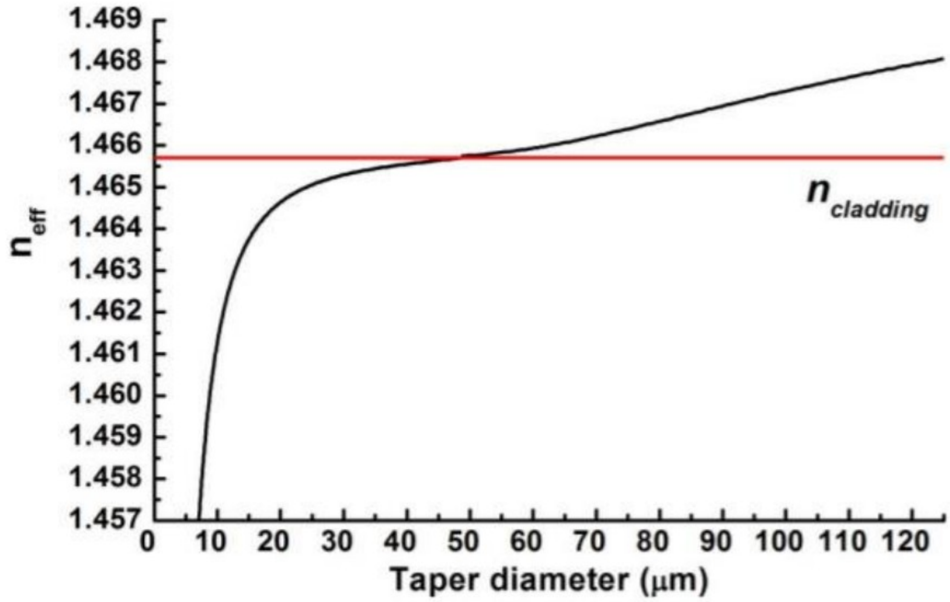

Figure 2.22: The change of n_{eff} with the variation of the taper diameter (Li et al, 2011).

2.4.5 Twist Sensing

The tapered fiber twist sensing is based on the power demodulation of the taper when it is subjected to rotation. Figure 2.23 shows a linear decrease of optical power as the taper is rotated from 0° to 35°. Tapered fiber is very sensitive to external perturbation especially bending. Twisting a taper will create a small deflection to the taper angle. Any small angle deflection ($\leq 10^{\circ}$) exerted to the taper will cause intrinsic leak of the fundamental mode resulting in a huge power variation of the transmitted light. As shown in Figure 2.24, the transmitted power drops significantly as the bending angle increases. However, when the bending angle exceeds 8.5°, the transmitted light becomes confined within the core instead of further escaping to the surrounding (Chan et al, 2020).

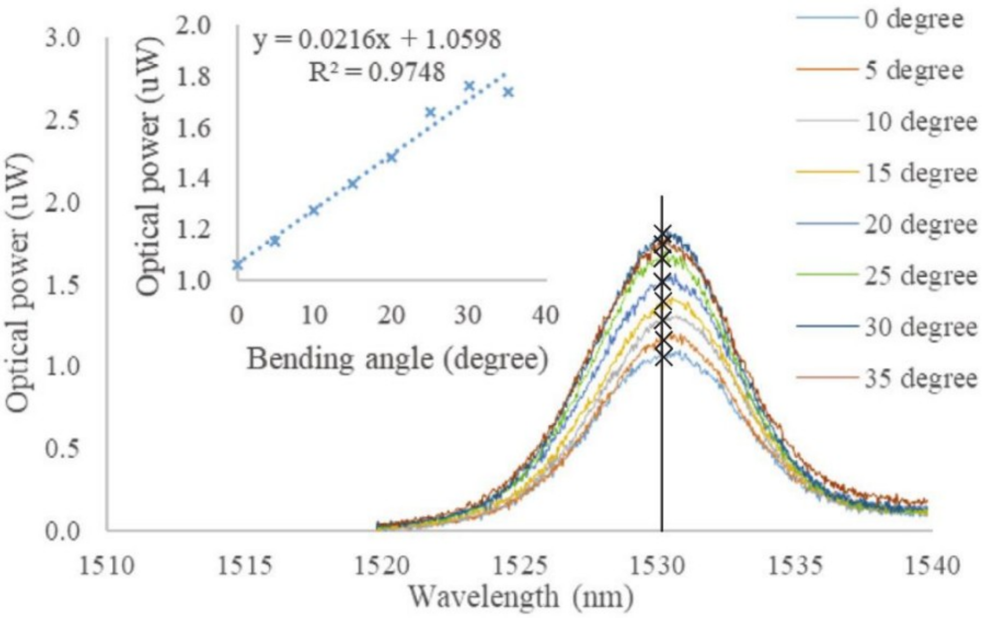

Figure 2.23: The optical power variation of the looped MZI when subjected to bending. (Png, 2018)

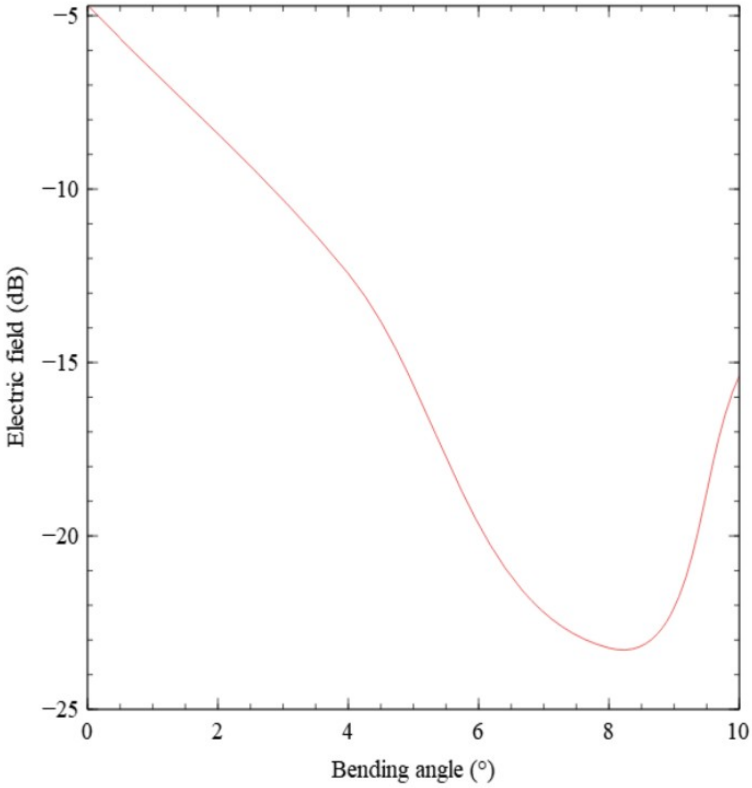

Figure 2.24: Simulation of power variation of the transmitted light across taper as the bending angle of the taper increase. (Chan et al, 2020)

CHAPTER 3

METHODOLOGY

3.1 Introduction

The methodology of this project comprises of three parts as shown in Figure 3.1. The first part is the application of optical sensor in SHM, where a packaged taper based in-line MZI sensor was used to conduct curvature measurement on a lab scale CFS roof truss. Second part of the methodology is the continuation of previous experiment, where a sensing array was developed to operate multiple MZI sensors simultaneously. In the last part of the project, a compact tapered fiber sensor with a built-in sub-carrier multiplexer was proposed. The experiment began with the design, fabrication, lastly followed by characterization. In the end of the experiment, the twist sensing and multiplexing capability of the sensor was experimentally verified.

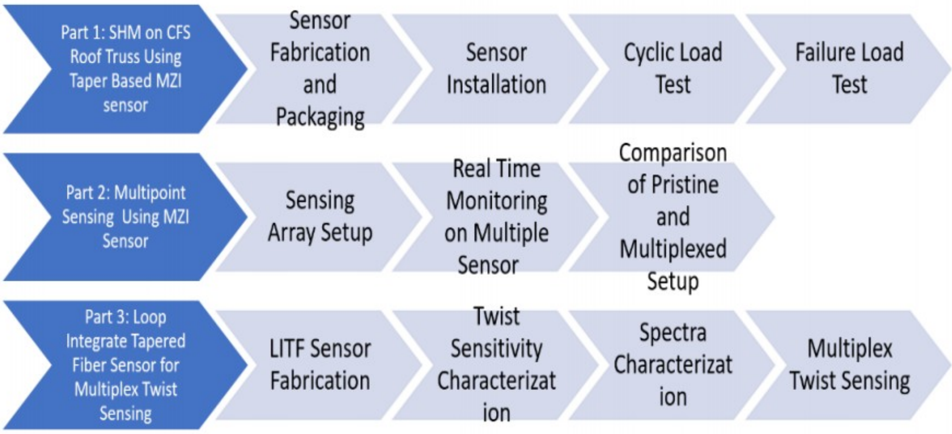

Figure 3.1: Outline of methodology.

3.2 Part 1: SHM on CFS Roof Truss

MZI fiber sensor is very sensitive in curvature sensing. The SHM application of MZI sensor on the roof truss can tell the overall health status of the structure by measuring the curvature change due to a deflection. The fragile nature of taper is a problem when it comes to curvature sensing. To use taper based MZI fiber as a curvature sensor, a proper packaging is needed to reinforce the tapered MZI fiber to survive in curvature measurement.

3.2.1 Sensor Fabrication and Packaging

The fabrication of the taper is done by using an in-house heat-and-pulling rig as shown in Figure 3.2. The fabrication rig uses electric arc as heat source, where the narrow hot zone of arcing will produce an abrupt biconical taper as shown in Figure 3.3. The pulling mechanism is controlled by a stepper motor.

After the arcing, a digital microscope was used to capture the microscopic image of the taper to analyze the profile. The sensitivity of the MZI sensor is highly rely on the taper waist diameter. In the previous experiment conducted by Png, the MZI sensor with 50 microns waist diameter achieved a sensitivity of 1.65 μW/km^{-1} (Png et al, 2018). With the capability of the existence pulling rig, 30 microns is the most suitable taper waist diameter size after compromise with the sensitivity and the fabrication difficulty. The pulling distance to create a 30 microns diameter taper was calculated by using equation (8).

Since the interference output of MZI sensor depends on the coupling and re-coupling of the light when it transmits through the taper, any small deviations in the taper profile, waist diameter and interferometer length can lead to a totally different optical spectrum. Unfortunately, with current fabrication techniques, it is impossible to perfectly replicate a taper. Therefore, the spectrum profile of each fabricated MZI fibers is unique. It is necessary to characterize each of them before implementing them in any test.

The packaging was done as shown in Figure 3.4. The tapered MZI fiber was sandwiched between two 7 cm ×1 cm × 0.1 cm polypropylene slabs using cyanoacrylate adhesive glue. The purpose of the double layer packaging is to provide a protection that is strong yet flexible enough to conduct curvature measurement in harsh monitoring environment as well as to reduce effect of ambient temperature on the sensor. Besides that, the sandwich packaging will make the entire structure more rigid, which will help the sensor return to its original state when the sensor is unbent (Raji et al, 2016; Png et al, 2018).

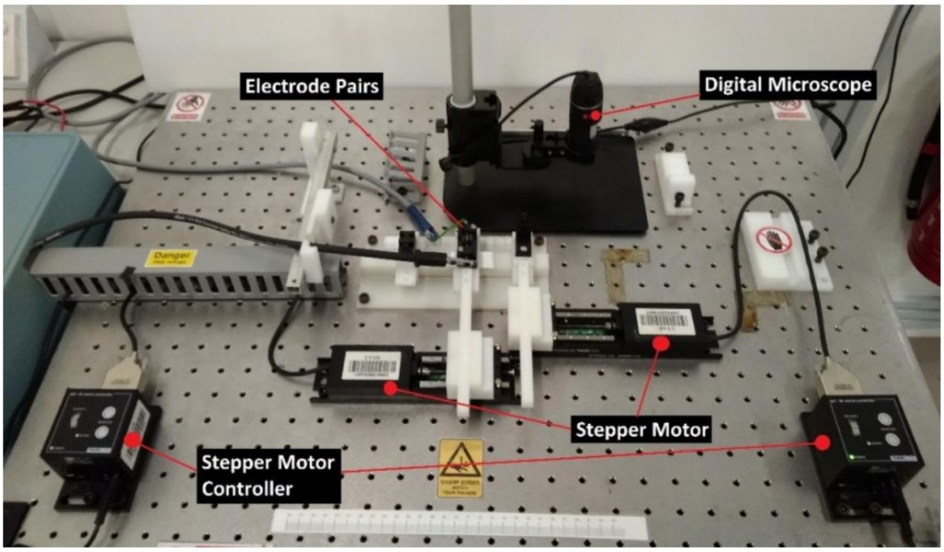

Figure 3.2: The image of self-made heat-and-pulling taper fabrication rig.

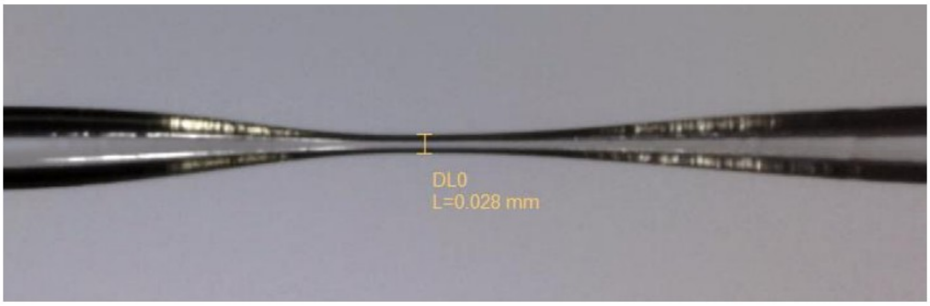

Figure 3.3: The microscopic image of a tapered fiber captured using a digital microscope under ×250 magnification.

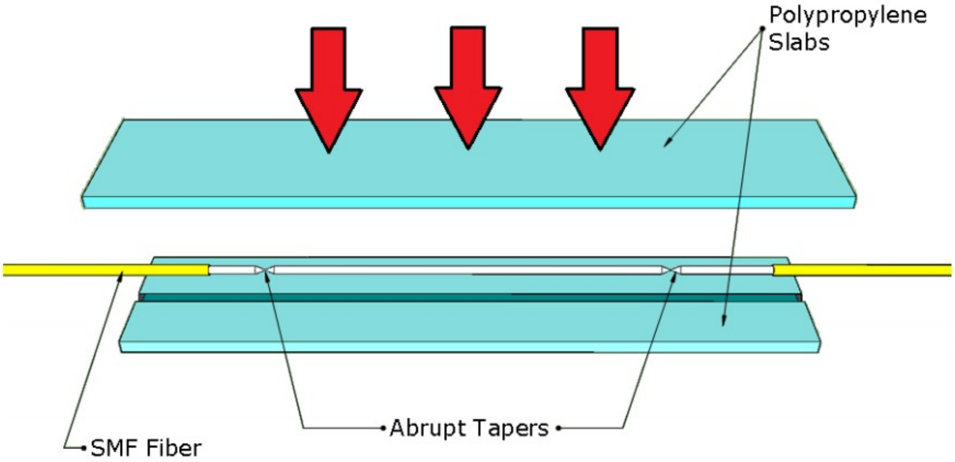

Figure 3.4: Schematic illustration of a packaged in-line MZI fiber

3.2.2 Designs of CFS Roof Trusses

Two different designs of CFS roof trusses with same dimension of 0.481 m × 2.891 m × 0.2 222m were used in the experiment. The illustration of the two different designs is shown in Figure 3.5. The first specimen is a conventional design truss where three web members were used to join the upper and bottom chord. The design of the second specimen is slightly different from the conventional design. Instead of having web members, two heel plates were used to strengthen the connection between two chords. Due to the enhancement from the heel plates, the load would distribute more evenly throughout the entire structure, which will result in a different deformation behavior compared to the conventional design (Dave et al, 2006; Gan et al, 2018). The purpose of using two different designs in load test is to determine the feasibility of MZI sensor under different circumstances.

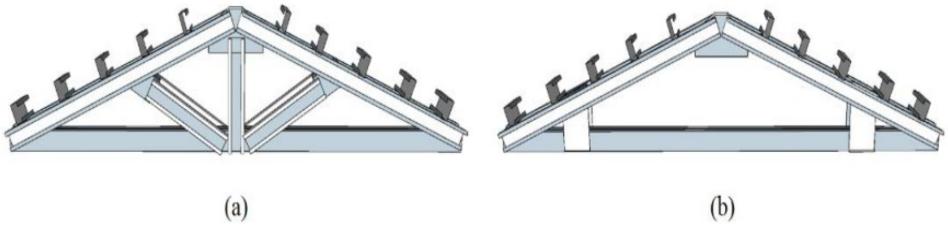

Figure 3.5: Illustration of CFS roof truss with (a) web members and (b) heel plates.

3.2.3 Load Test Setup and Sensor Installation

The experiment setup is shown in Figure 3.6. The specimen was placed on top of two cylinder supports and vertically loaded at the center top by using a hydraulic jack. A packaged MZI sensor was attached to the midspan of bottom chord by means of cyanoacrylate adhesive as shown in Figure 3.7. A linear vertical displacement transducer (LVDT) was installed next to the MZI sensor to measure the exact value of the vertical deflection, *d* of the bottom chord for calibration purpose. The data collection was done by using a data logger for LVDT and a commercial optical loss test set (OLTS) for MZI sensor. The installation of the sensor was done one day before the load test to let the adhesive dry completely so that the sensor was bonded strongly to the chord's surface.

The actual curvature of the bottom chord was computed by using equation (13), where *C* is the curvature, *d* is the vertical deflection of bottom chord and *l* is the span between two cylinder supports, which is 2 meters.

$$\mathrm{C} = \frac{8d}{4d^2 + l^2} \tag{13}$$

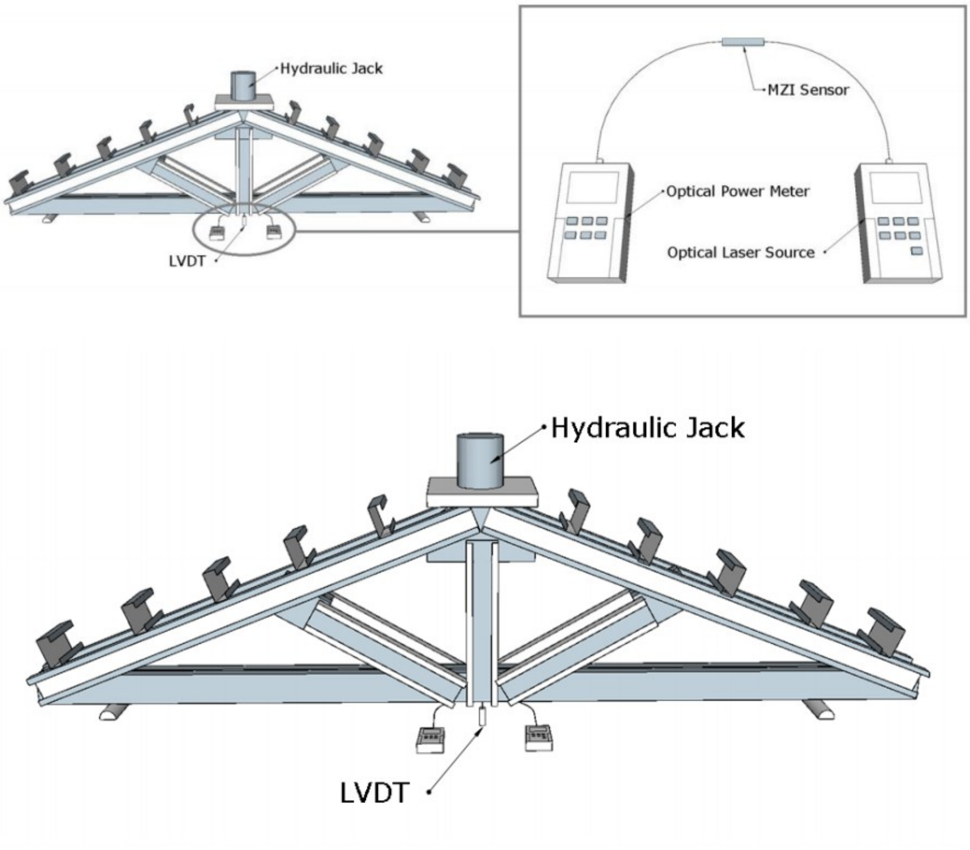

Figure 3.6: Illustration of three-point bend test on CFS roof truss using hydraulic jack and the setup of MZI sensor.

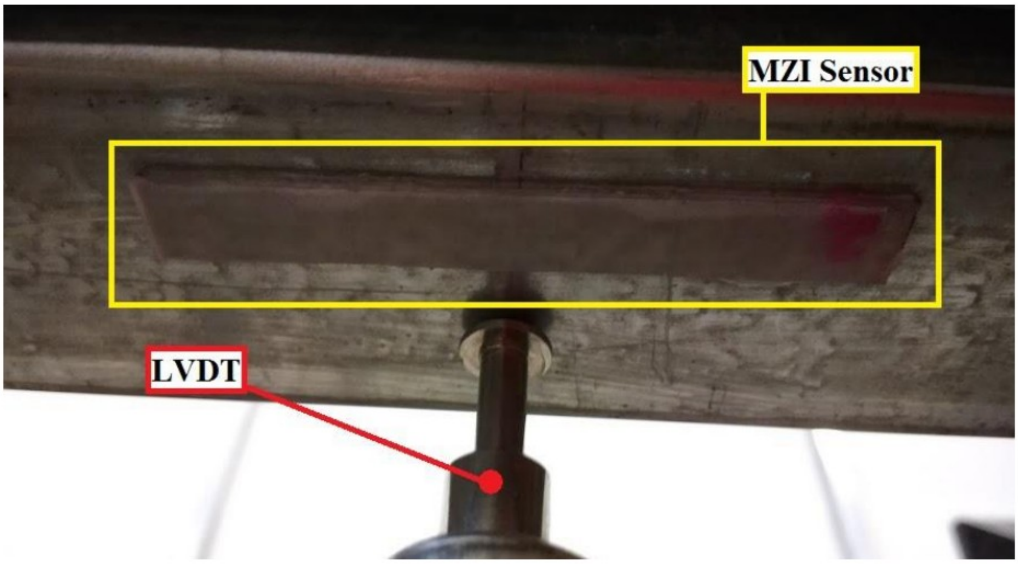

Figure 3.7: The installation of MZI sensor and LVDT under the bottom chord.

3.2.4 Load Test

In the cyclic loading test, the first specimen (with web members) was subjected to a vertical load with an increment of 1kN loading force per step. Optical power readings of the MZI sensor output with different operating wavelengths (1310 nm, 1490 nm and 1550 nm) and the LVDT were recorded at every step. A few load cycles were conducted by repeatedly extruding and releasing the load force on the specimen. The first load cycle was conducted within the load force of 8.5kN to 12kN, which was repeated twice. The second load cycle was repeated within the range of 12kN to 15kN. Following this, the specimen was loaded until the truss had reached its ultimate bearing capacity, where structural deformation happened.

In the failure load test, the setup of the experiment was the same with the previous one except the second specimen was used. The second specimen (with heel plates) was subjected to constant increase of load with 1kN force per step until the truss met its failure. The readings of MZI sensor and LVDT were recorded.

3.3 Part 2: Multipoint Sensing Using MZI Sensor

3.3.1 Setup of Sensing Array

The MZI sensing arrays experiment setup was illustrated in Figure 3.8. Two packaged in-line MZI sensors (sensor 1 and sensor 2) were attached to the midspan of a 1 m long hardened steel bar and aligned parallel next to each other as shown in Figure 3.9. A commercial optical laser source was used to provide a 1550 nm wavelength and -2.0 dBm optical input. A 3dB coupler was used to split the source equally into both MZI sensors. The other ends of the two MZI sensors were connected to photodetectors and the sensing signal was retrieved through a digital oscilloscope (PicoScope 2000).

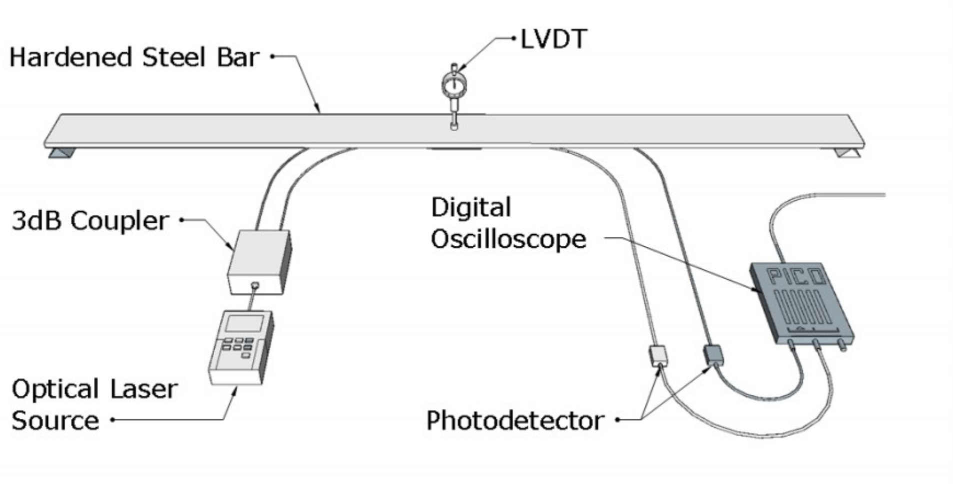

Figure 3.8: Illustration of the sensing array setup.

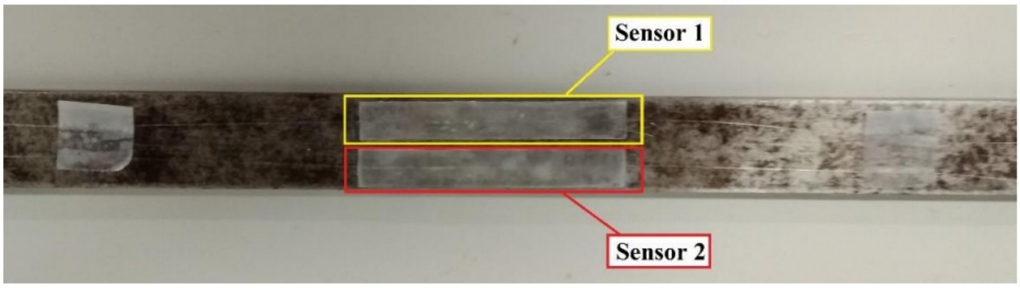

Figure 3.9: Installation of two MZI sensors on the hardened steel bar.

3.3.2 Real Time Monitoring on Multipoint Load Test

The steel bar was loaded by exerting 200g per step at the midspan. Vertical deflection of the steel bar was recorded through an LVDT. The curvature of the steel bar was computed using equation (13).

A real time monitoring was done to observe both MZI sensors' outputs when the steel bar was subjected to load. The output power changes of both sensors were converted into electrical signal and then recorded by a digital oscilloscope with the sampling interval of 163.8μs and 6.104kS/s sampling rate for every measurement. Each step was recorded for a period of 5 seconds. The average optical intensity was computed from the repeated data and the normalized optical intensity against the curvature was plotted using MATLAB for further analysis.

The experiment was repeated with the same procedure but with a pristine setup where only one sensor was involved. The 3dB coupler was removed and sensor 1 was connected directly to the laser source. The result of pristine setup was compared to the multiplexed setup to determine the attenuation of sensor sensitivity due to the presence of 3 dB coupler.

3.4 Part 3: Multiplex Sensing of Twist Sensor Using SCM

In this section, an optical twist sensor integrated with a sub-carrier multiplexer was demonstrated. By utilizing the twist and bend sensitive taper, the sensor was able to conduct twist measurement and sub-carrier multiplexing simultaneously. In SCM sensing array, each sensor was assigned a specific sub-carrier signal through acoustic modulation for discrimination purpose.

3.4.1 Working Principle of Looped-Integrated Tapered Fiber Sensor

The looped-integrated tapered fiber (LITF) sensor is proposed to carry out twist sensing and sub-carrier multiplexing simultaneously with a single optical device. The design of LITF sensor is modified based on the looped-integrated MZI sensor originally proposed for acoustic vibration detection (Png, 2018). But instead of acoustic sensing, the acoustic sensing element is used as an acousto-optic modulator (AOM) to modulate the desired frequency into the transmission light through acoustic vibration.

The schematic illustration of LITF sensor is shown in Figure 3.10. It has a similar structure to the in-line MZI except a loop segment is integrated in between two tapers. The purpose of coiling the fiber is to remove the interferometric effect from the output. Since there are two tapers in the sensor, if the separation between two tapers is close enough, the surviving cladding mode will re-couple into HE_{11} mode forming an interference output. The FSR spectrum will interfere with the transmission power of the sensor and increase difficulty of the observation. According to a study done by Ong et al. (2017), the bending radius of the loop should not be smaller than 10 mm to avoid unnecessary bending loss. Another purpose of the loop is to serve as a torque. The twisting of taper can be done easily by rotating the loop along the fiber without the need to add in extra rotation element.

During the operation, the sensor was actively modulated with a specific sub-carrier frequency through an external acoustic source. The sub-carrier signal is modulated into the HE_{11} mode through the periodic vibration of the tapers. When it was subjected to twist measurement, power demodulation will be induced in the HE_{11} mode according to the twist angle. As a result, the LITF sensor will generate an intensity modulated with a specific sub-carrier frequency.

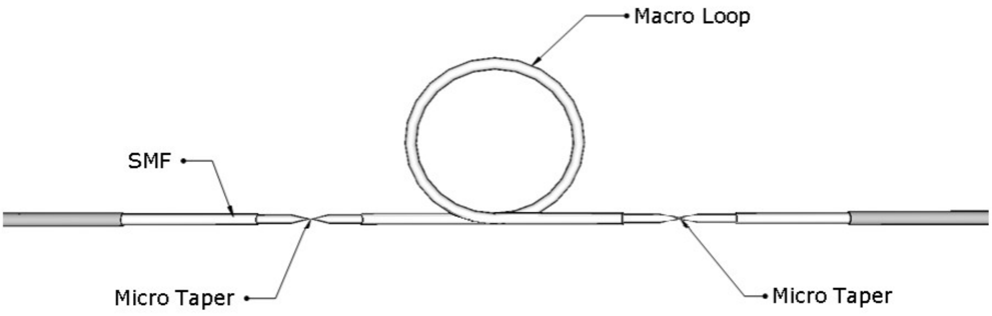

Figure 3.10: Schematic illustration of LITF sensor.

3.4.2 LITF Sensor Fabrication

The procedure of looped SMF-28 fiber fabrication is shown in Figure 3.11. An SMF-28 fiber was coiled into a loop and the junction was temporarily held in place by paper tape. The diameter of the loop was adjusted to 2 cm and a tiny amount of cyanoacrylate adhesive was applied on the tape and allowed to dry completely. The solid residue of the adhesive will fix the junction and held the loop structure tightly.

Next, one micro taper was created 3 cm away from the loop at each side using the same fabrication technique as mentioned in section 3.2.1. The taper waist diameter of both tapers was around 40 microns.

A sample of the LITF sensor is shown in Figure 3.12(a). A well fabricated tapered loop fiber was fixed on the sensing arm (yellow region) with the loop pointing upward. The dimension of the t-shape slab is shown in Figure 3.12(b). The 0.3mm thick base slab was to enhance vibration sensing by minimizing the absorption of vibration from the measurand surface. During measurement, the sensor will be attached to the measurand surface through the coupling arms (green regions). The purpose of the coupling arms is to avoid the direct attachment of the sensing arms to the measurand surface, so that the tapered fiber mounted on sensing arms is free to vibrate at resonance to amplify the acoustic modulation (Soh, 2018).

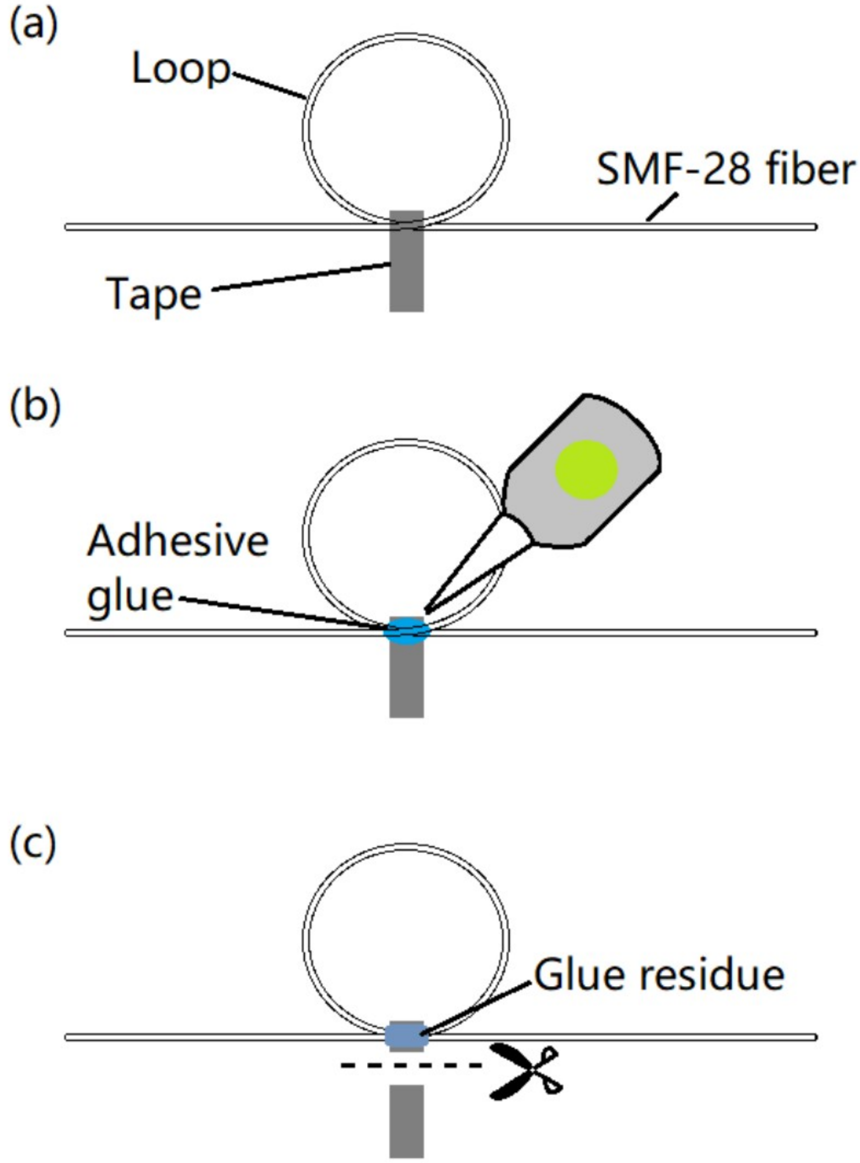

Figure 3.11: Fabrication procedure of the looped fiber. (a) A SMF-28 fiber was bent into a loop and fixed in shape with paper tape. (b) A few drops of adhesive glue were applied to the tape after the size of the loop diameter was adjusted. (c) Excessive tape was removed after the glue had completely dried.

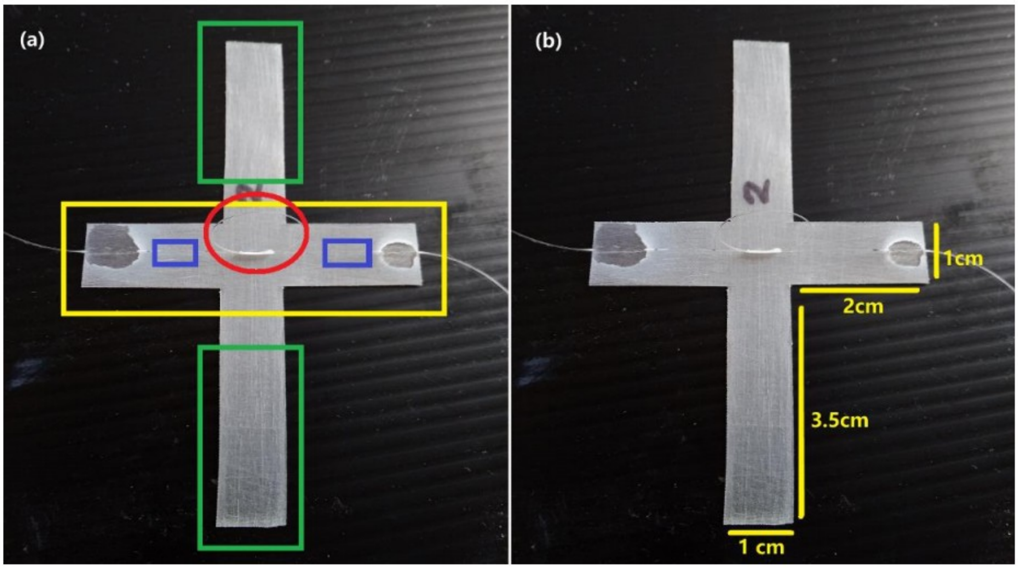

Figure 3.12: (a) Captured image of the tapered loop fiber fixed on the t-shape polypropylene slab, where the yellow region is the sensing arm, green regions are the coupling arms, blue regions show the positions of the tapers and red region is the loop. (b) The dimension of the sensor base slab.

3.4.3 Characterization on Twist Sensitivity

Three different configurations of looped fiber were fabricated as shown in Figure 3.13. These looped fibers were fixed on a flat board with the loop perpendicular to the surface. The experiment setup is shown in Figure 3.14, where an optical spectrum analyzer (OSA) was used to analyze the changes of the spectrum of three looped fibers when the loop was twisted. The output spectra of the looped fibers were recorded at loop angles 0°, 30°, 60°, 90°, 120°, 150° and 180°.

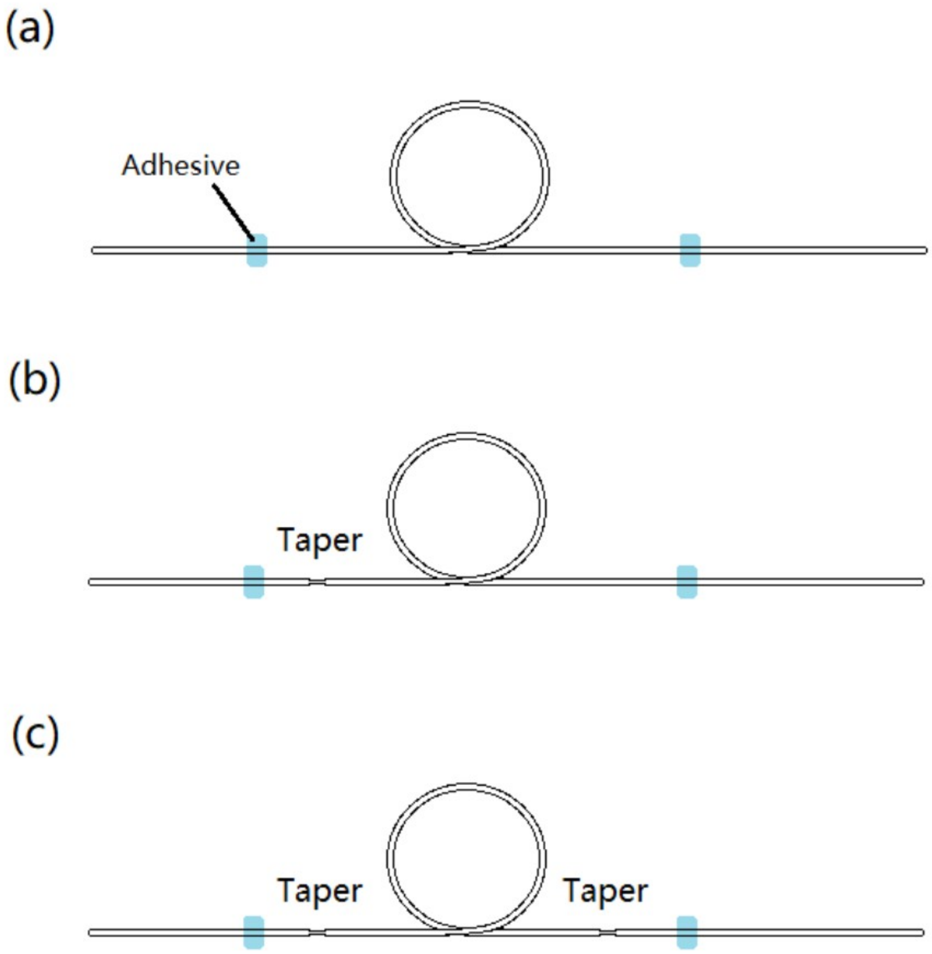

Figure 3.13: Configuration of the looped fibers (a) without taper, (b) with single taper, (c) and two tapers.

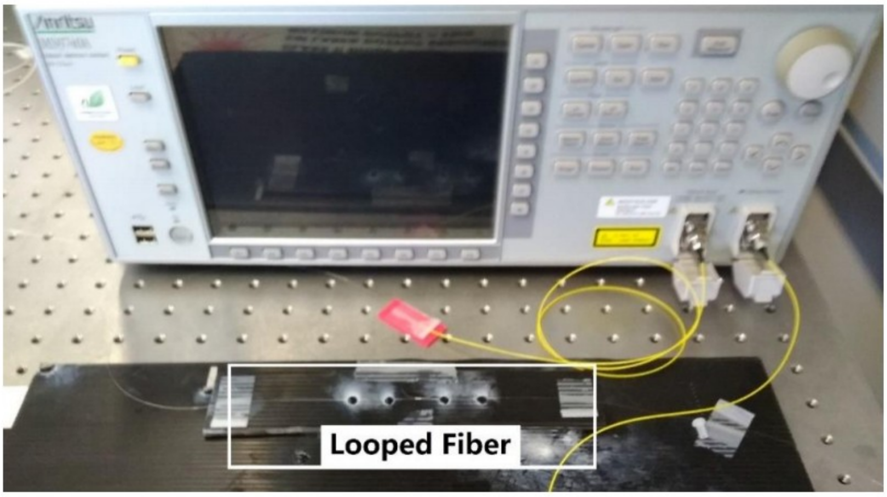

Figure 3.14: Experiment setup for twist sensitive characterization.

3.4.4 Characterization on Sensor Output Spectra

The spectrum of the LITF sensor is affected by the structure of the micro tapers and the loop. Any small deviation in the size of taper's waist diameter, taper shape profile and the loop's diameter will lead to a completely different output spectrum. Since a perfect replicate of the sensor is almost impossible with current fabrication techniques, each fabricated LITF sensor will have a different spectrum profile and a unique optimum operating frequency.

The characterization test was set up as shown in Figure 3.15. The input of the sensor was connected to a commercial optical laser source (-5.0dBm power, 1550nm wavelength) and the output was connected to a photodetector to convert the optical signal into electrical signal before passing it to digital oscilloscope (PicoScope 2000) for data analysis. The LITF sensor was attached on the diaphragm of a commercial speaker unit which acted as an acoustic source. The acoustic vibration was generated and controlled by a function generator with 5V peak-to-peak output. The generated vibration frequency was varied from 50 Hz to 3000 Hz and the results were recorded by the dedicated software for the digital oscilloscope, PicoScope 6.

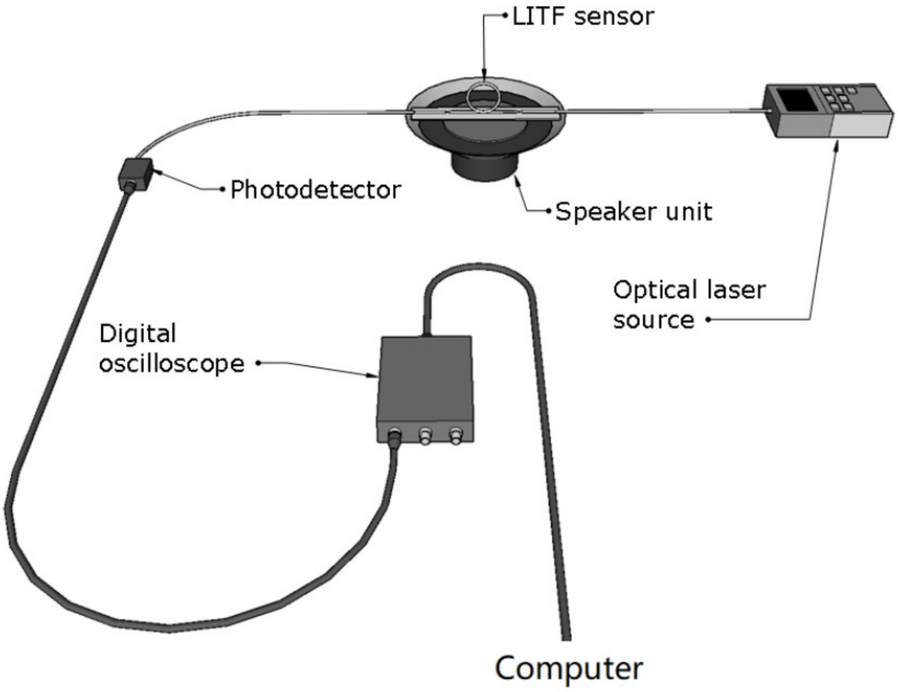

Figure 3.15: Setup of spectra characterization test.

3.4.5 Setup of SCM Sensing Array

Both LITF sensors were mounted on top of a 3-inch 4 ohms speaker unit's diaphragm as illustrated in Figure 3.16. Both sensors were powered by individual optical laser source with the same input of -5 dBm optical power and 1310 nm wavelength. The frequencies of the sub-carrier signals modulated to the sensors were 300 Hz and 250 Hz respectively. The output signals from both sensors were combined through a 3dB coupler and connected to a photodetector, where the signals were retrieved by digital oscilloscope. Since the frequencies of two peak signals are different, the signals from two sensors are distinguishable in the output overlapping spectra.

On top of the stepper motor, a platform with a vertical extended rod was mounted to twist the LITF sensor by exerting lateral force to the fiber loop.

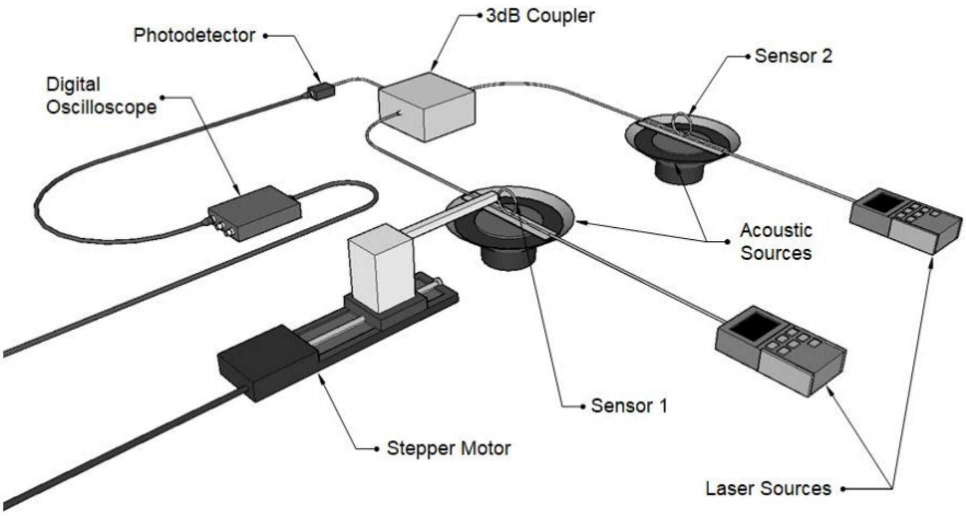

Figure 3.16: Schematic illustration of SCM sensing array with two LITF sensors.

3.4.6 Multiplexed Twist Sensing

A vertical force was exerted on the sensor 1 loop from the lateral direction as shown in Figure 3.17. The angle deflection, α of the loop was calculated from the vertical displacement, d through simple trigonometry calculation. In the first test, sensor 1 was subjected to twist measurement while sensor 2 remained at 0°. The reading of both sensors for every 0.1 mm step was recorded. The experiment stopped at d = 1.5mm as twisting the taper further might damage the sensor. To ensure both sensors function correctly in the sensing array, the test was repeated by switching the roles of sensor 1 and sensor 2. The twist measurement was repeated with sensor 2 and the readings of both sensors were recorded.

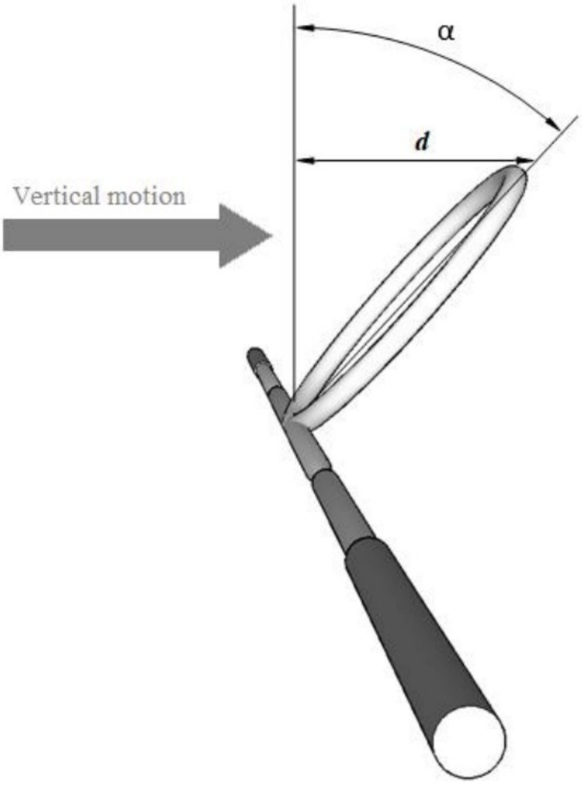

Figure 3.17: Schematic diagram of the LITF sensor twisted at angle α when a vertical force is exerted from the lateral direction.

CHAPTER 4

RESULTS AND DISCUSSIONS

4.1 Curvature Sensing on CFS Roof Truss Using Tapered Sensor

In both the cyclic load test and failure load test, two different design specimens were loaded with hydraulic jack until the specimens met their failures at 19kN and 30kN load force respectively. Due to the different structural designs, the second specimen lasted longer in the load test compared to the first specimen. The structural failures were determined through observation of deformation and the load feedback from the reaction frame control unit. The observation records of the deformation are shown in Figure 4.1.

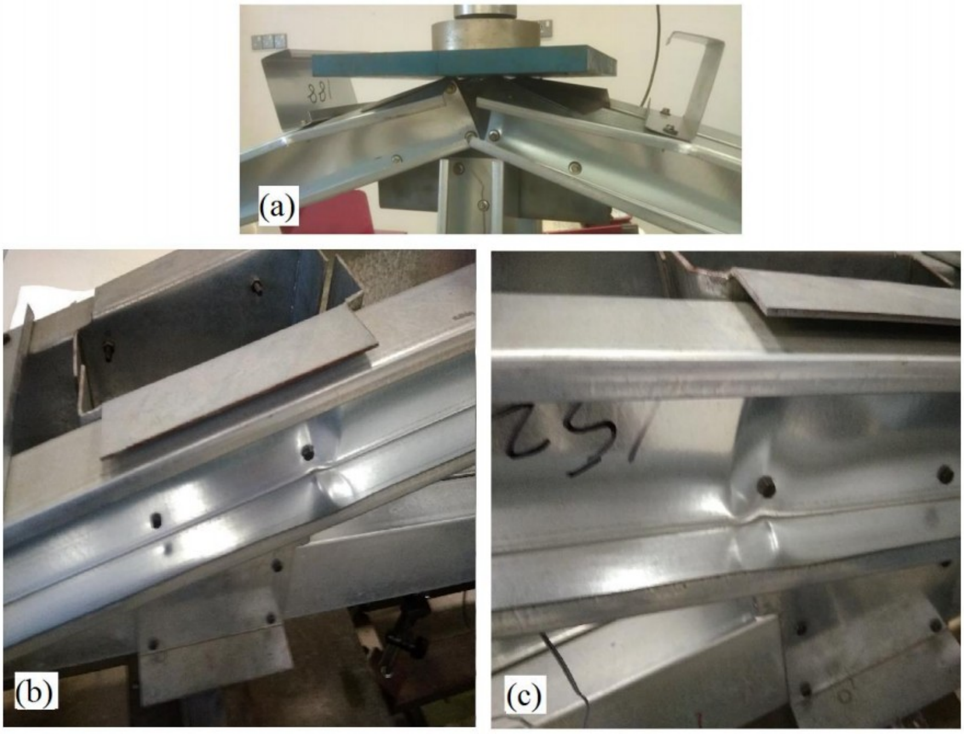

Figure 4.1: The failure of first specimen happened at (a) top chords. Second specimen failure occurred at (b) left heel connection and (c) right heel connection.

4.1.1 Operating Wavelength Characterization

Figure 4.2 shows the optical powers readings of MZI sensor taken from first specimen load test with three different operating wavelengths (1310 nm, 1490 nm and 1550 nm). The differences in the linearity and the up-down trend of the linear curves of three operating wavelengths were due to the difference in FSR shifting in different wavelength. The results showed that the MZI sensor had the highest sensitivity of -3×10^{-5} μW/N and highest linear regression coefficient, R^2 of 0.8592 at 1550 nm. Whereas the sensitivity of MZI sensor is lowest at 1490 nm but high linearity and the sensitivity at 1310 nm is close to 1550 nm but the linearity is lowest. Both sensitivity and linearity are important criteria for MZI sensor as they are affecting the sensor's accuracy in measurement and calibration. Thus, the data of 1550 nm operating wavelength with best sensitivity and linearity was selected for further analysis in the next section.

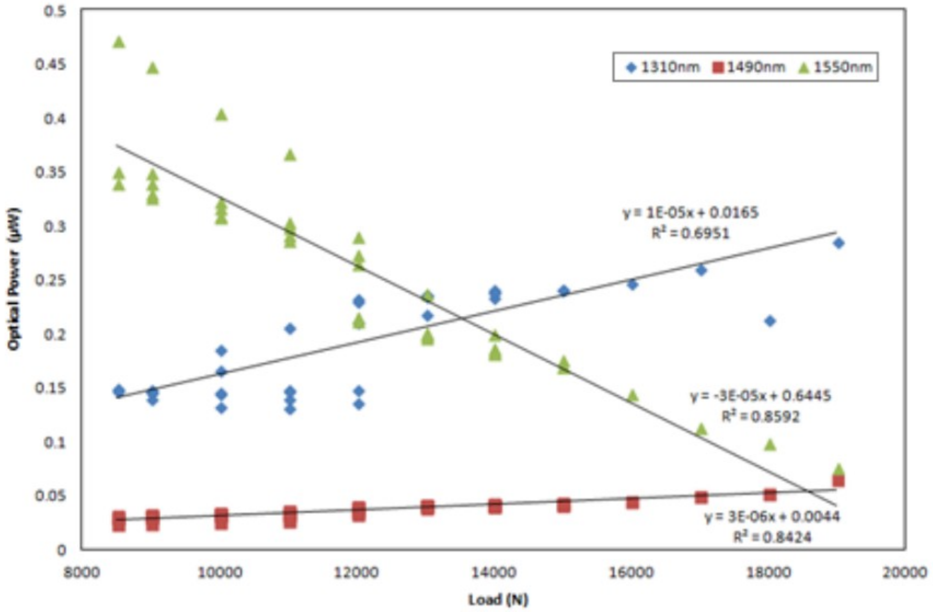

Figure 4.2: MZI sensor optical power outputs during the load test when using optical laser source at 1310 nm, 1490 nm and 1550 nm wavelengths.

4.1.2 Cyclic Load Test Results

Figure 4.3 shows the mapping of the MZI sensor and the LVDT sensor during the first specimen loading test with a good regression value r^2 of 0.9876. The correspondent relation between the optical power and curvature change is governed by the linear equation of the slope. The respondent optical powers of MZI sensor were converted to curvatures and plotted against the loading force. As shown in Figure 4.4, the maximum curvature changes per

1kN detected by MZI sensor is 0.8524 km^{-1} and minimum change is 0.2488 km^{-1}.

The cyclic tests were conducted at different load ranges. During the load test, the specimen was loaded and unloaded twice from 8.5kN to 12kN load range. After the data was collected, the specimen continued loaded and performed another cycle at higher load from 12kN to 15kN. The reasons of splitting the cyclic load procedure into multiple cycles is to prevent the data collection of the cyclic loading is interrupted if the specimen failed in the middle of long-range one-cycle load test. Since the specimen met its failure at 19kN, it interrupted further cyclic tests. The average curvatures of the first and second cycles were sub-plotted in Figures 4.5(a) and 4.5(b) to show a clearer comparison. The deviation of MZI sensor results compared to LVDT in both cyclic tests were less than 5% which indicated the repeatability of MZI sensor is precise and reliable. Note that the first attempt of loading the specimen in both cyclic tests was not included in the average value. This is because the deformation of metal screws connection under heavy load caused the specimen’s failure to return to its original state after first attempt. Thus, it is excluded for a more reliable repeatability test result. The three load attempts of first and second cyclic tests were shown in Figure 4.6, where the first attempt for each test was indicated by a blue dotted line.

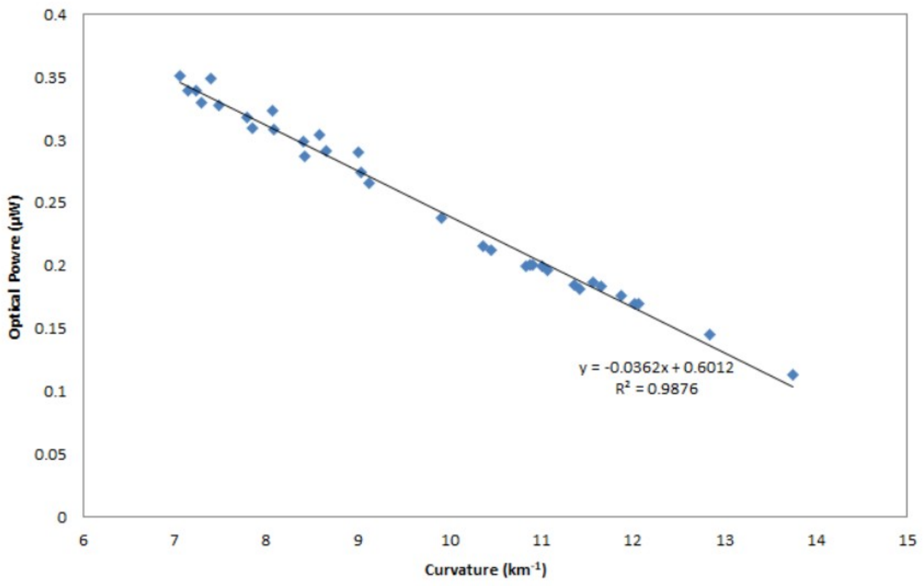

Figure 4.3: The curvature reading of the MZI sensor is calibrated through the mapping of MZI sensor's optical power to LVDT's calculated curvature.

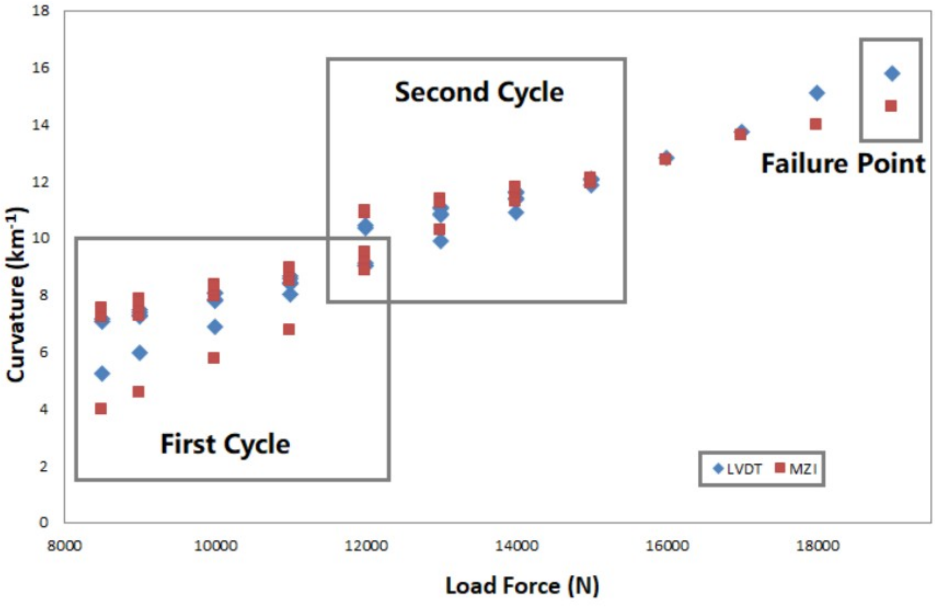

Figure 4.4: The load test comparison between MZI sensor and LVDT.

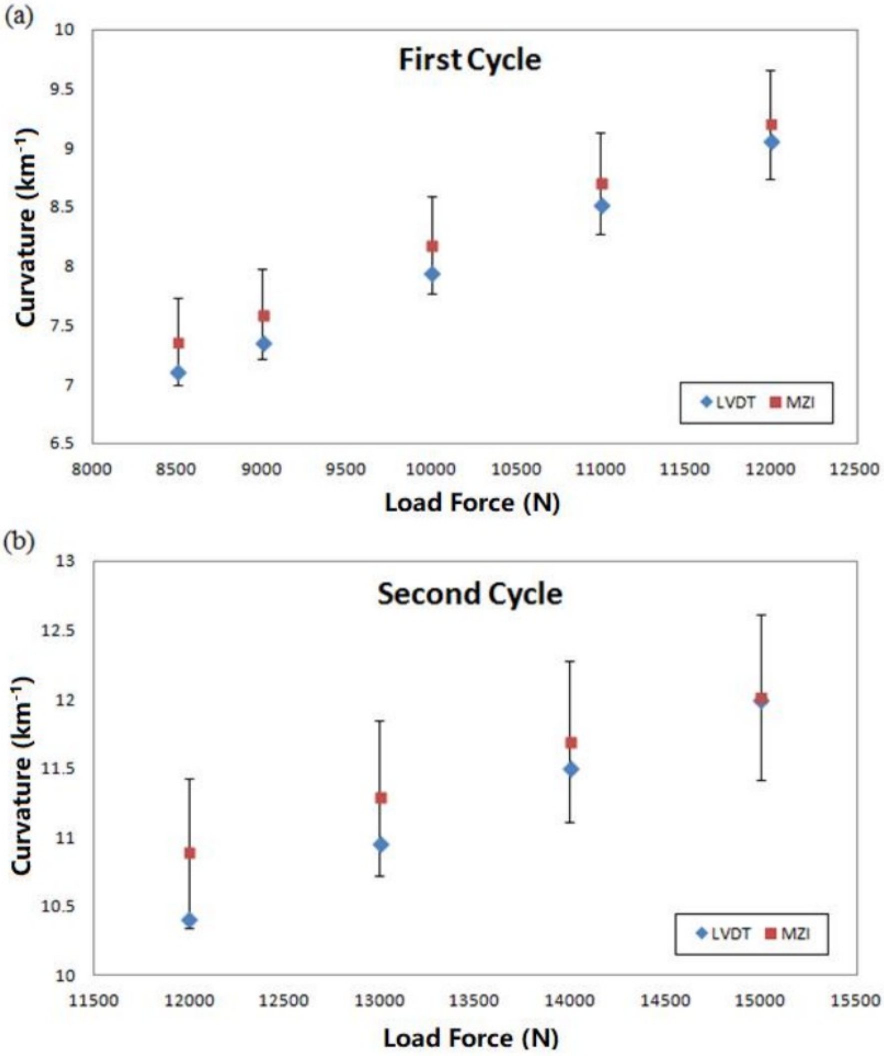

Figure 4.5: The average values of the curvature readings during cyclic load tests at (a) first cycle and (b) second cycle with ±5% deviation between MZI and LVDT.

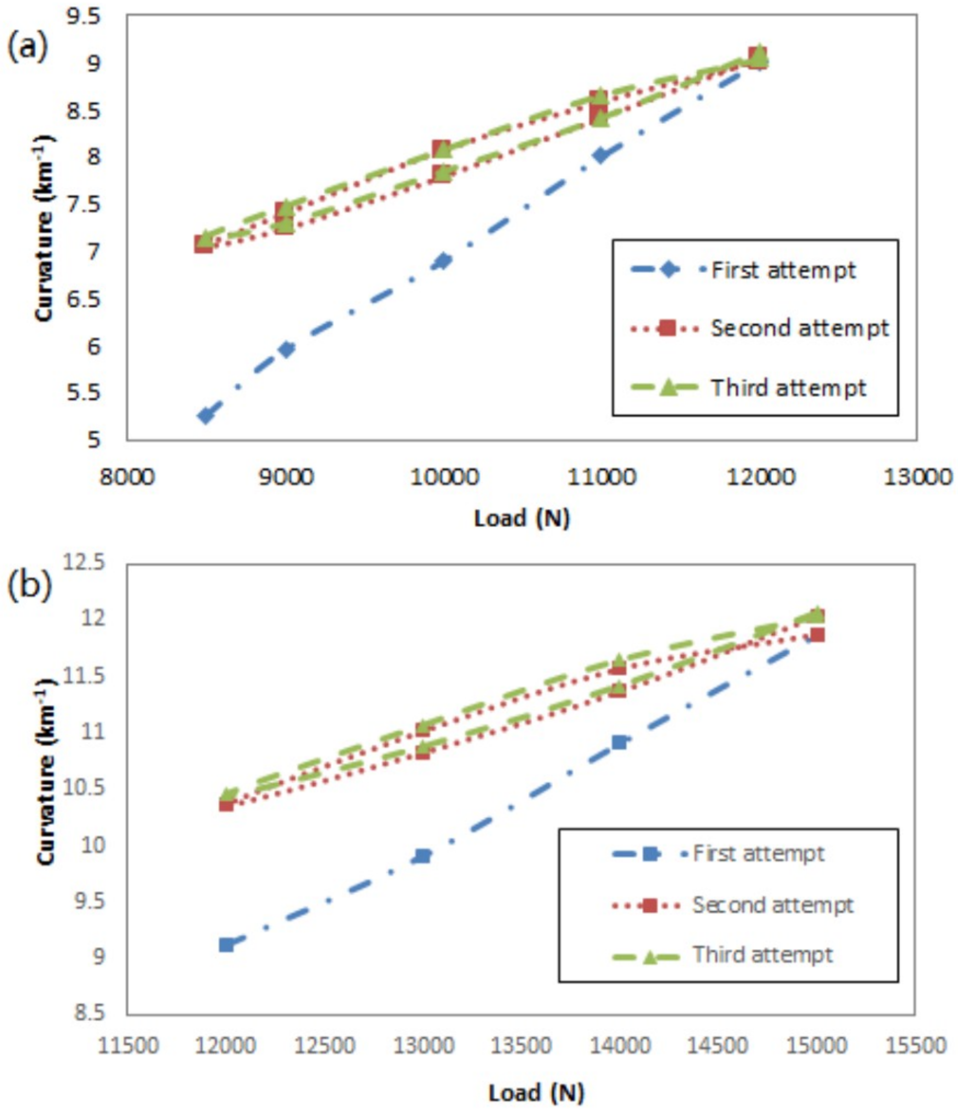

Figure 4.6: The average values of (a) first and (b) second cyclic test was taken from second and third attempts.

4.1.3 Failure Load Test Results

In the second load test, the same procedure in section 4.1.1 was carried out on the second specimen with heel connection and the optimum operating wavelength for this MZI sensor was 1490 nm. The correspondent relation between the optical power and curvature was determined through the mapping shown in Figure 4.7. During the load test, MZI sensor detected a linear increase in curvature with maximum and minimum curvature changes at 0.15174 km^{-1} and 0.07304 km^{-1} respectively. The full-range curvature change is shown in Figure 4.8, where the curvature change is again mapped against LVDT for verification. The overall deviation between the MZI sensor and LVDT sensor results is within ±3%. Curvature of the truss decreased linearly until a reverse trend happened at 29kN, as both MZI sensor and LVDT detected the same structural deformation on the specimen.

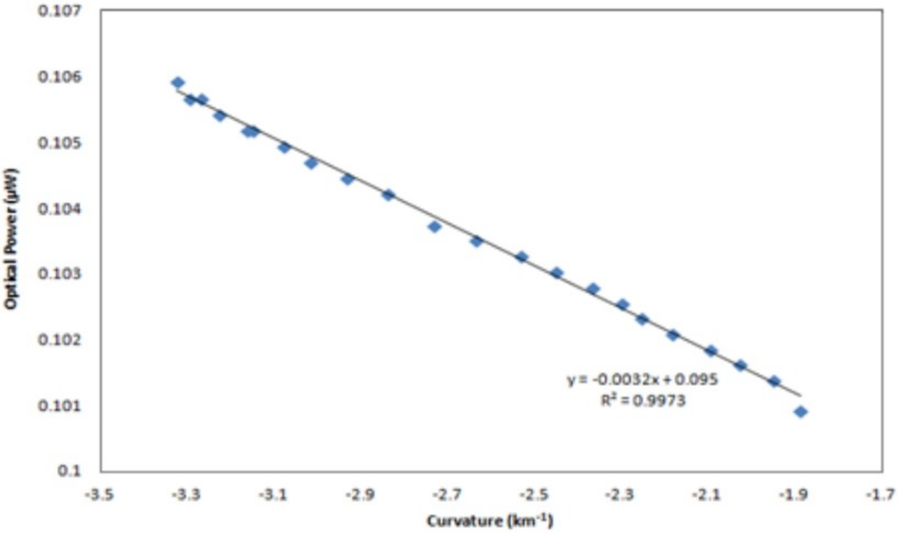

Figure 4.7: Graph of optical power from MZI output versus curvature from LVDT on second truss throughout the entire loading process.

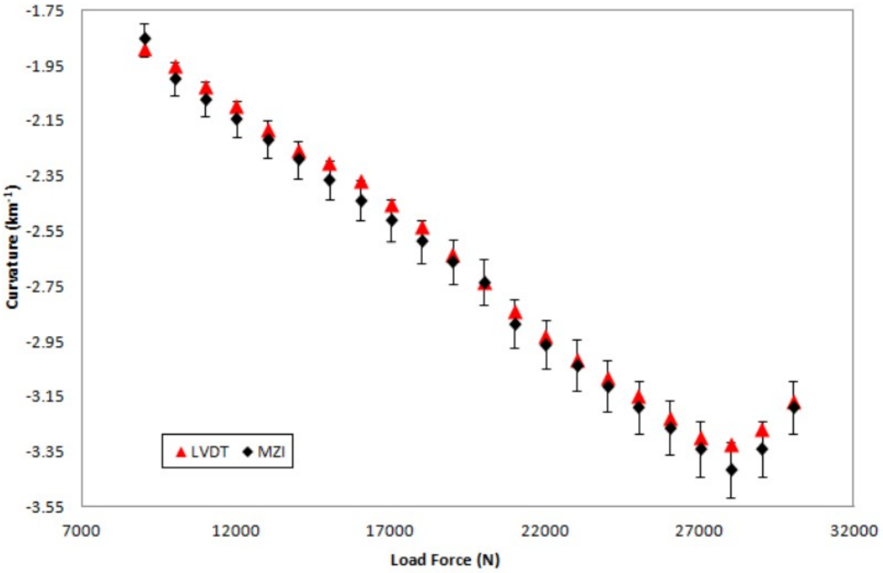

Figure 4.8: The comparison between MZI sensor and LVDT in the load to failure test with ±3% error bars.

4.1.4 Discussion

In this part, both the feasibility and repeatability of MZI sensor on CFS roof truss have been proven. The performance of MZI sensor has shown a very high agreement with that of the conventional LVDT sensor on both trusses. In cyclic load tests, the average percentage error of the repeatability sensing is ±5%. Whereas in the failure load test, the MZI sensor had achieved a sensitivity of 0.0032 $\mu W/km^{-1}$ (3.2 $\mu W/m^{-1}$) within the range of 1.880 km^{-1} to 3.324 km^{-1} and the MZI sensor deviation from conventional LVDT sensor is ±3%.

4.2 Multipoint Sensing Using SDM

4.2.1 Simultaneous Sensing with Two MZI Sensors

Figures 4.9(a) and 4.9(b) show the results of multipoint sensing with two MZI sensors voltage ratio change when subjected to an identical curvature change. A best fit line was shown on both graphs, and the regression coefficients, r^2 of both graphs are 0.9763 and 0.9835 respectively, showing that both sensors responded linearly to the curvature change. The upward/downward trends and sensitivities of both linear curves are different due to the unique spectrum profile of in-line MZI fiber. The sensitivity of sensor 1 and 2 obtained in this experiment are 25.095 dB/km and 29.1 dB/km.

To verify the reliability of sensors 1 and 2, the optical powers of the respective sensors after unloading were compared to the initial optical powers. Table 4.1 shows the comparison of optical powers of sensor 1 and 2 before and after the curvature tests where only minute percentage differences of 4.6% and 1.9% were observed. This indicates the sensors' repeatability in the SDM sensing array is reliable and the results are replicable.

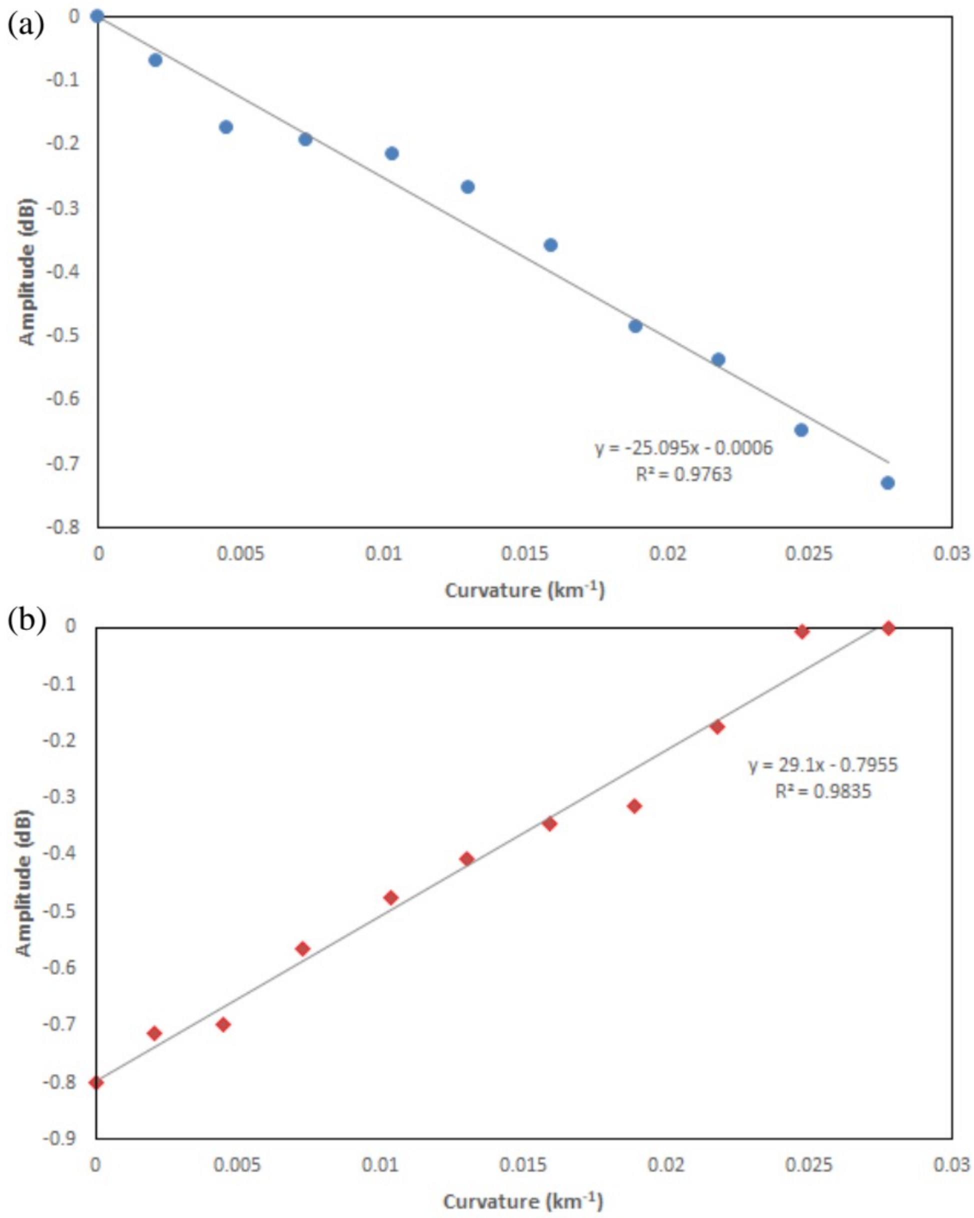

Figure 4.9: The normalized power variation of (a) sensor 1 and (b) sensor 2 when the steel bar was loaded.

Table 4.1. Comparison of sensor output power ratio before and after the curvature test.

	Amplitude (dB)		
	Before	***After***	***Percentage Difference***
Sensor 1	0	0.045926	4.6%
Sensor 2	0.79905	0.78357	1.9 %

4.2.2 Comparison of Pristine and Spatial-Division Multiplexed Setup

Attenuation is a major issue in multiplexing system as it might compromise the sensitivity of sensors when a splitter or coupler is involved. An experiment was done to address this issue to compare the sensor response with and without incorporating a splitter or coupler to an SDM system. A pristine MZI sensor experiment was set up where no coupler was involved and only sensor 1 was used in the measurement. The comparison of pristine setup and multiplexed setup corresponding to the curvature is shown in Figure 4.10. The sensitivity of the sensor 1 in pristine setup is -23.307 dB/km, which is only 7.6% difference compared to the -25.095 dB/km in multiplexed setup.

Figure 4.11 illustrated the mapping of optical power between the individual sensor and the multiplexed sensor. The regression coefficient, r^2 of the mapping has achieved a percentage of 96.06%. This indicates the parallel sensing configuration did not affect the pristine power of the sensor and is reliable to be implemented in multiple points sensing.

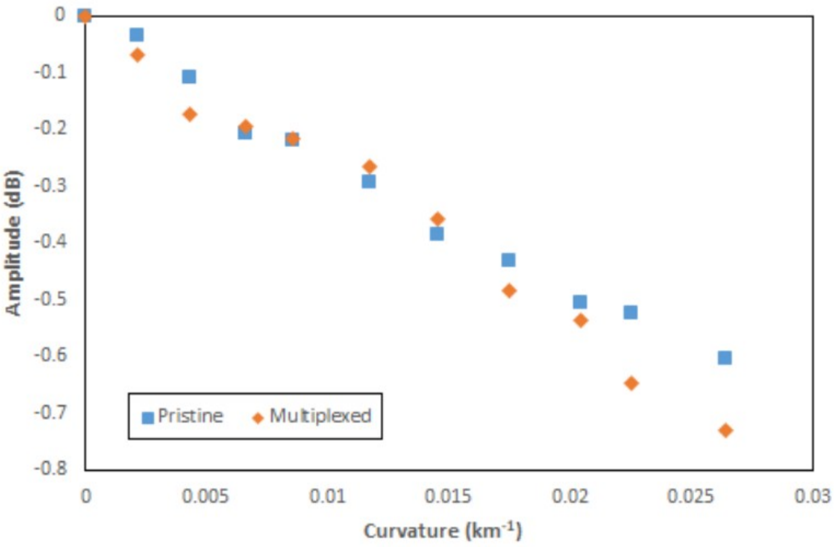

Figure 4.10: The comparison of sensor 1's response in pristine setup and multiplexed setup corresponding to the curvature change.

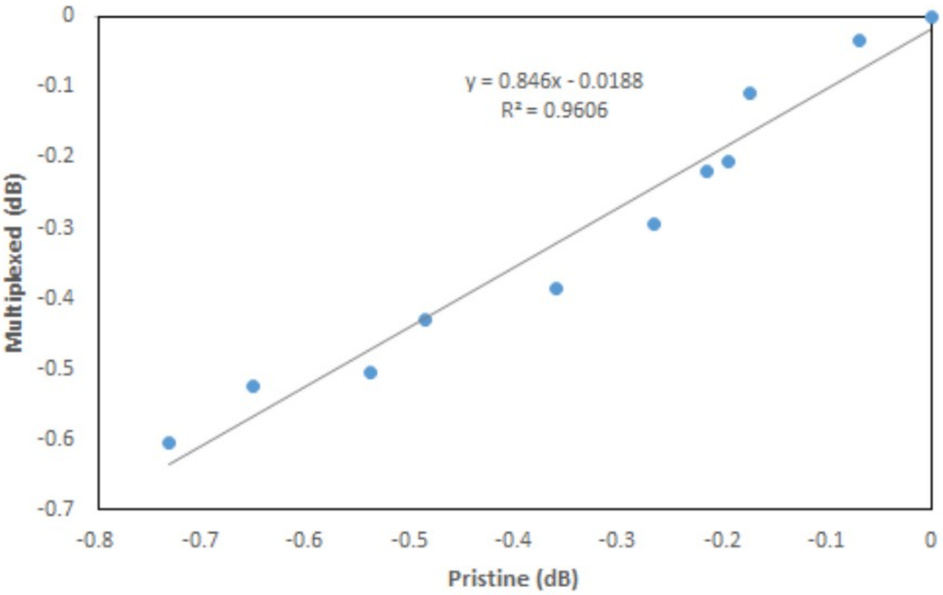

Figure 4.11: Mapping results of the pristine and multiplexed setup.

4.2.3 Discussion

A simple, direct and effective way to operate multiple MZI sensors was demonstrated by using parallel topology. A real time monitoring of two MZI sensors was demonstrated, and the feasibility was verified.

The attenuation of signals in the parallel sensing array was insignificant. The regression coefficient, r^2 of mapping between pristine and multiplexed setups is 0.9606, indicating that the curvature measurement of MZI sensor in pristine and multiplexed setup is high resemblance.

4.3 Twist Sensing Using Two LITF Sensors

4.3.1 Twist Sensitivity Characterization

The effect of the taper on twist sensitivity was characterized. Three different configurations of looped fibers with single taper, double taper and without taper were subjected to twist measurement from 0° to 180°. The measurements were recorded by using an optical spectrum analyzer (OSA) and the spectrum profiles are shown in Figure 4.12.

Figure 4.12(a) shows the maximum power variation of looped fiber without taper is 0.53 dB when the loop was twisted from 0° to 180°. When more than one taper was introduced to the looped fiber, the variation of the output power increased significantly. The maximum power variations of single taper and double taper configuration are 7.96 dB and 12.16 dB respectively as shown in Figures 4.12(b) and Figure 4.12(c).

This characterization results show that the twist sensitivity of the looped fiber is related to the number of tapers fabricated along the fiber. When no taper was involved, the power variation was almost negligible because the twist sensitive component was absent. Double tapered looped fiber was more sensitive in twist sensing compared to single tapered fiber. Therefore, the double taper configuration was adopted in the design of LITF sensor.

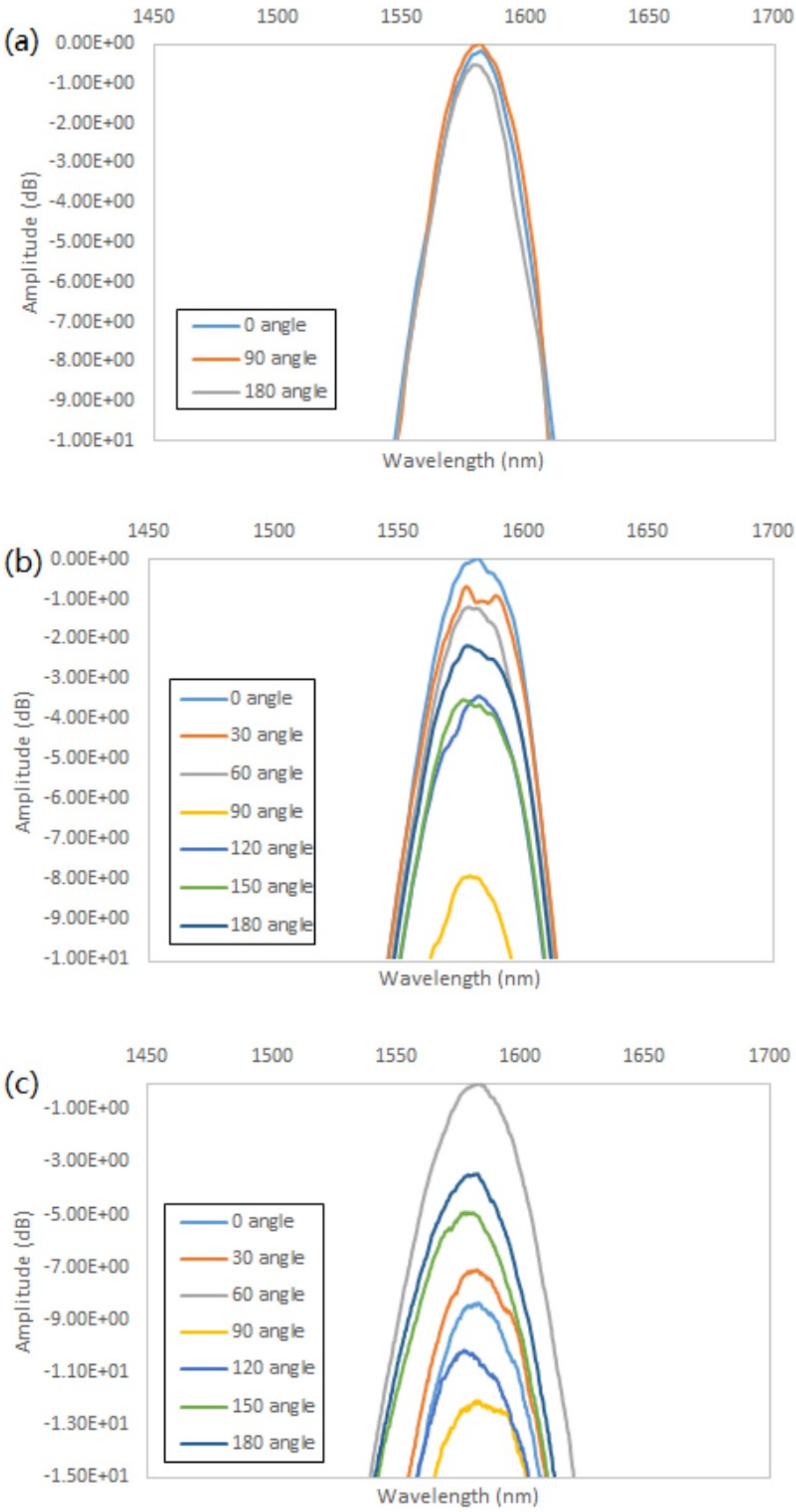

Figure 4.12: The spectrum profile of (a) no taper, (b) single taper and (c) double taper looped fiber when subjected to twist measurement.

4.3.2 Spectral Characterization

Figure 4.13 shows the spectrum profile of a LITF sensor when modulated with signal frequency from 50 Hz to 3000 Hz. When the sensor was subjected to low frequency vibration, the amplitude of the peak signal was highly sensitive to the modulated frequency but at the same time the spectrum will be overwhelmed by unwanted harmonics peaks. When it comes to overlapping spectrum, it is necessary to ensure that the peak signals from multiple LITF sensors do not overlap with other signal peaks and harmonics peaks. Therefore, the operating frequency should be higher than 250 Hz.

When the frequency was above 500 Hz, the peak signal amplitude no longer dropped as the modulated frequency increased. An enlarged view of spectra when modulated with frequencies from 1.4 kHz to 3.0 kHz is shown in Figure 4.14. The amplitude is the highest when modulated with 1.6 kHz while the lowest at 2.0 kHz. The physical resonance of the sensor's base slab is responsible to the fluctuation of the amplitude. As shown in Figure 4.14, the highest point of the nine peaks forms a slowly descending sinusoidal wave trend. During the characterization measurement, the vibration of the sensor's base slab is overlapped with the sensor peak signal forming an addition output of both sensor and the slab. Similar phenomenon is observed in Png's looped MZI sensor that have similar structure design where the amplitude at certain frequencies is differ from the overall trend (Png et al, 2018). This phenomenon is only obvious when the peak signal amplitude is low. Thus, it is not observed in the low frequency range when the amplitude of the sensor signal is relatively high.

For a better sensitivity during the measurement, the peak amplitude of the operating frequency needs to be as high as possible. In the characterization, the usable frequencies with peak amplitudes higher than 20 dB were recorded.

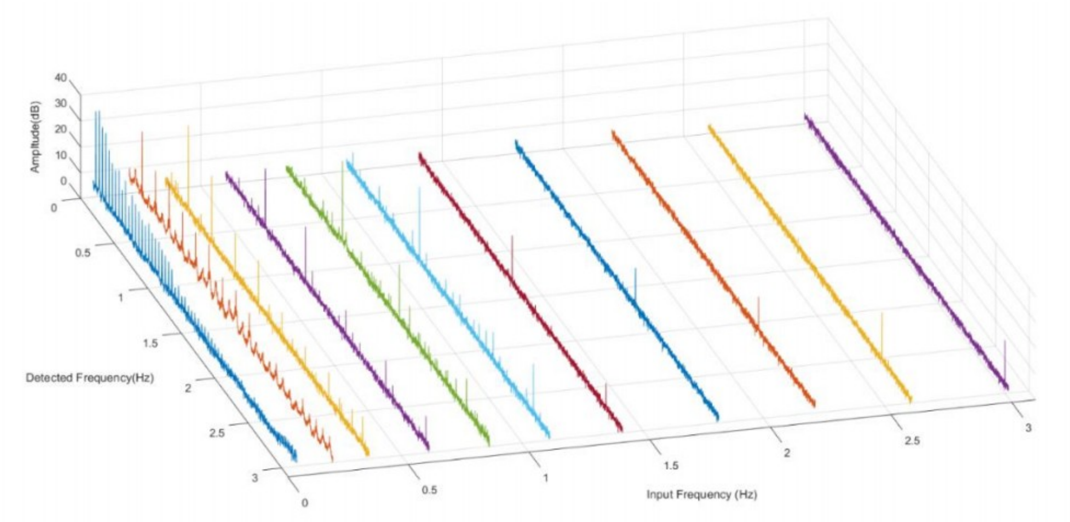

Figure 4.13: Spectrum characterization from 50 Hz to 1000 Hz.

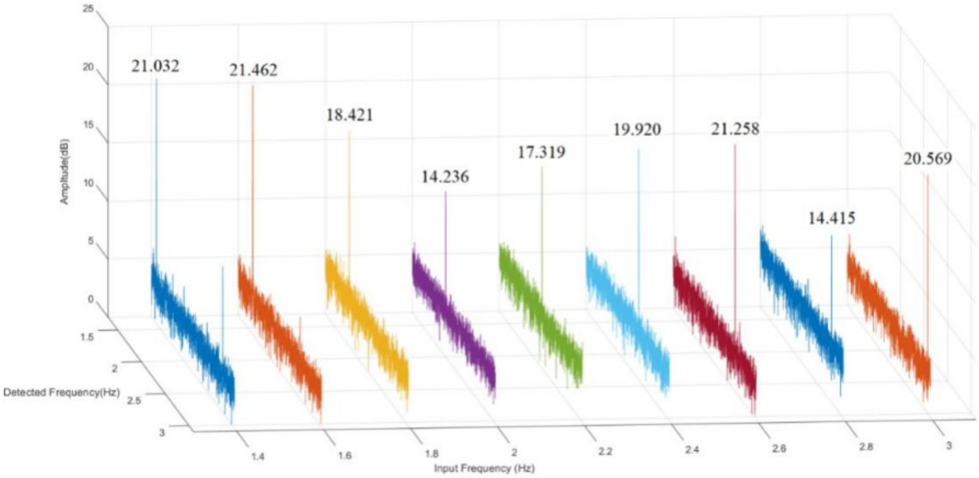

Figure 4.14: The spectral responses of the sensor when modulated with 1.4 kHz, 1.6 kHz, 1.8 kHz, 2.0 kHz, 2.2 kHz, 2.4 kHz, 2.6 kHz, 2.8 kHz and 3.0 kHz.

4.3.3 Comparison of Pristine and Sub-Carrier Multiplexed Setup

Since the multiplexed array included a 3dB coupler, the output power transmitted from both LITFs will be reduced by half as they passed through the coupler. The reduce in power intensity might compromise the sensitivity of the sensors. Thus, a comparison of LITF sensor in pristine and the multiplexing systems was done to determine the attenuation effect of the multiplexing system to the sensor.

Figure 4.15(a) show the mapping results of the LITF sensor in pristine and multiplexed setup. The coefficient of determination, R^2 of 0.9867 shows there is a high resemblance between these two sets of results. The trends of both variables are shown in Figure 4.15(b). The figure shows that both trends are highly alike except the power of the multiplexed setup is lower than the pristine setup, which is reasonable due to the presence of the 3dB coupler. The attenuation of the power due to multiplexing system is relatively small in signal-to-noise-ratio (SNR), which was less than 20% reduction as shown in Figure 4.16.

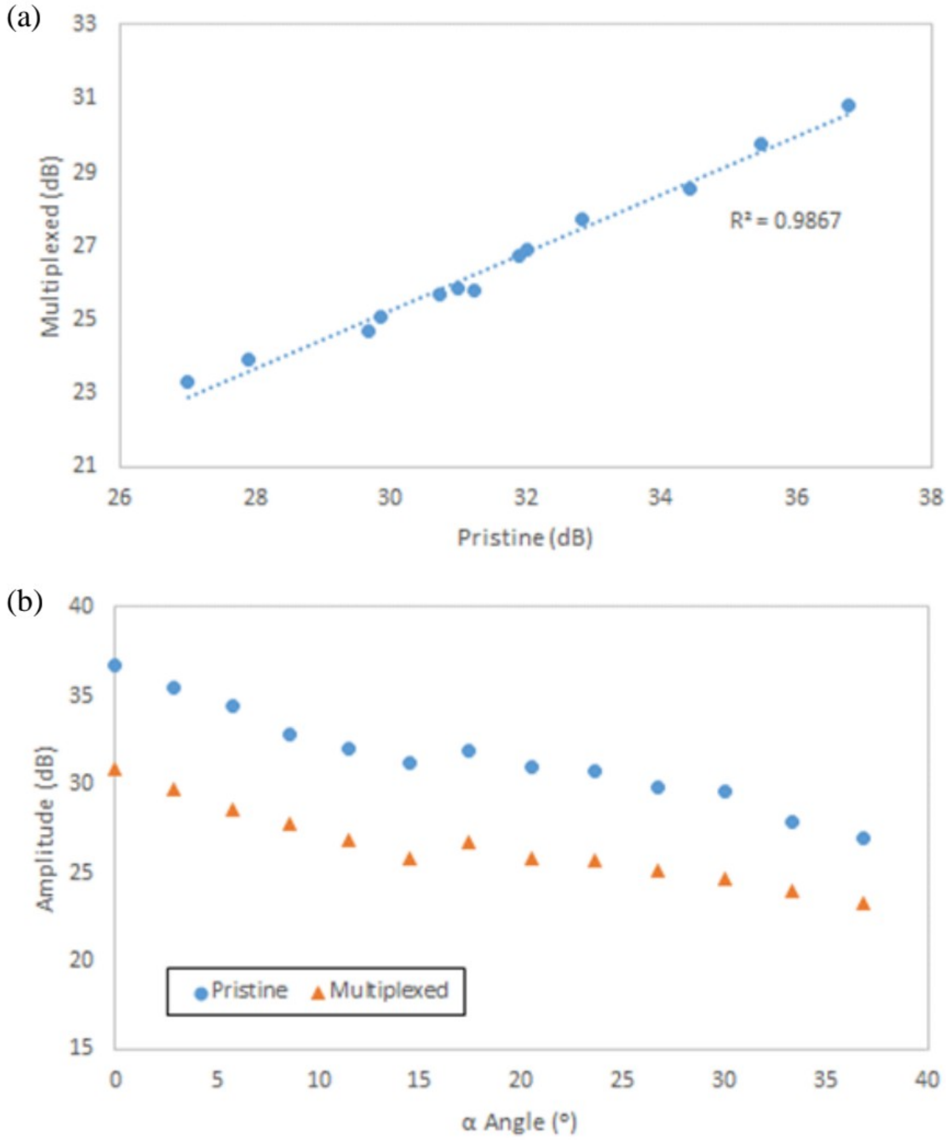

Figure 4.15: (a) The mapping results of the pristine setup and multiplexed setup. (b) The pristine and multiplexed power change when the torsion angle α was twisted from 0° to 36.8°

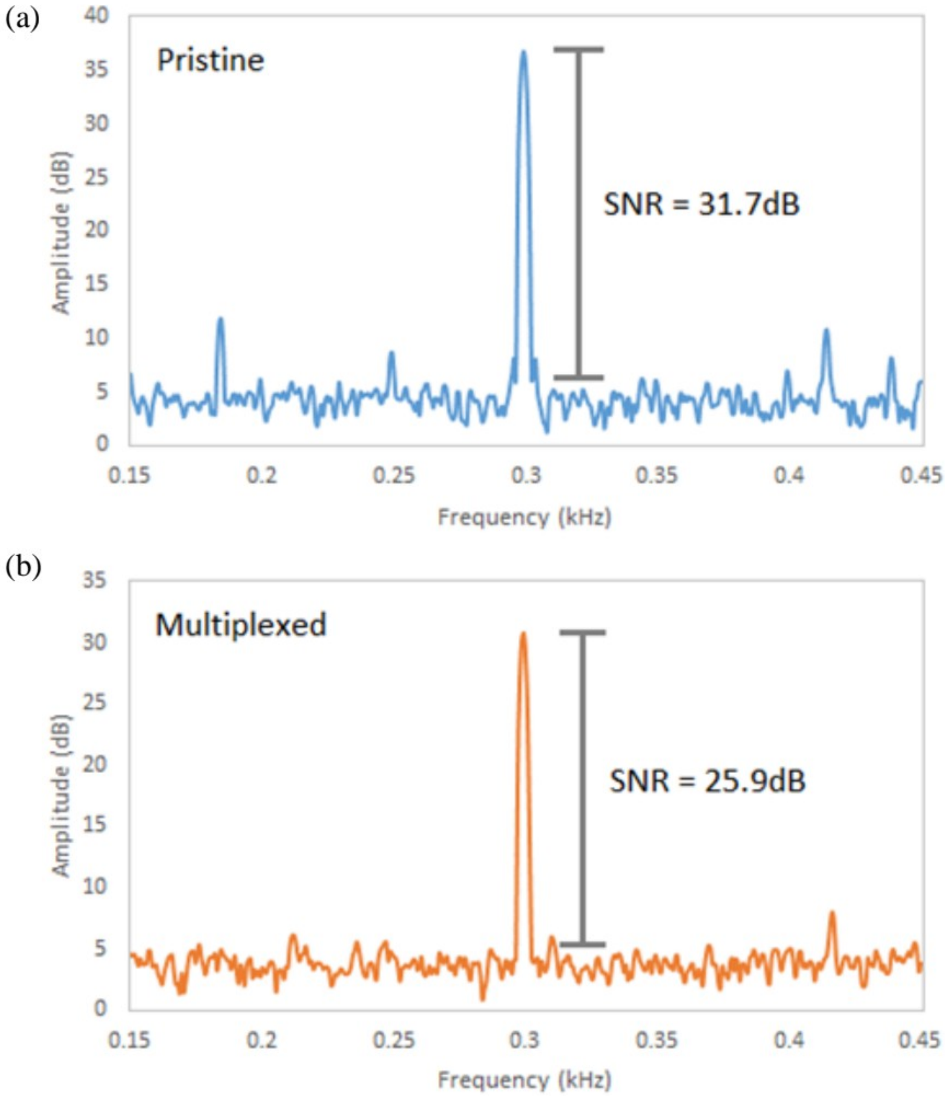

Figure 4.16: SNR of the (a) pristine signal and (b) multiplexed signal when α angle was 0°.

4.3.4 Twist Sensing Array Using SCM

The overlapping spectra of two LITF sensors at rest are shown in Figure 4.17, where the first peak at 250 Hz represents the sensor 1 output and second peak at 300 Hz represents sensor 2.

In the first test, the loop's torsion angle α of sensor 1 was varied from 0° to 36.8° steadily by the stepper motor with 1 mm per step. Meanwhile, the torsion angle of sensor 2 remained static at 0°. The results of both sensors are shown in Figure 4.18(a). The graph shows that the output of sensor 1 dropped as the torsion angle α increased. The high regression value r^2, 0.9891 indicates that the power decreased in a highly uniform trend, whereas the output of sensor 2 shows a negative trendline with a small gradient of -0.0118 dB/°.

To ensure both sensors in the multiplexed system were functioning correctly, the twist measurement was further evaluated by switching the roles of sensor 1 and sensor 2. As shown in Figure 4.18(b), the output amplitude of sensor 2 increased as the loop was twisted. The r^2 value of 0.9258 is slightly lower compared to the sensor 1 and the trend of amplitude change was reversed. This is due to the different spectrum profiles of the LITFs resulted from the taper fabrication process. When the loop was twisted, micro-bending that happened at the taper might cause more light to escape or confine within the core depending on the structural configuration as stated in section 2.4.4.

An interrelation of crosstalk effect was observed in both tests. The plots in Figure 4.18 show that the amplitude change occurred gradually for sensor 2 in test 1 and sensor 1 in test 2, although they remained static throughout the twist measurement. The rates of amplitude change for both un-twisted sensors are -0.0118 dB/° and 0.0153 dB/° respectively. Another phenomenon observed was the trends of amplitude change of un-twisted sensors were the same as the test sensor. Both sensors showing negative trend in test 1 and positive trend in test 2 indicated that the amplitude of the un-twisted sensor was influenced by another sensor in the same sensing array. This unintelligible crosstalk is due to the intermodulation distortion (IMD), where unwanted coupling happened when two or more modulated signal channels were combined into one.

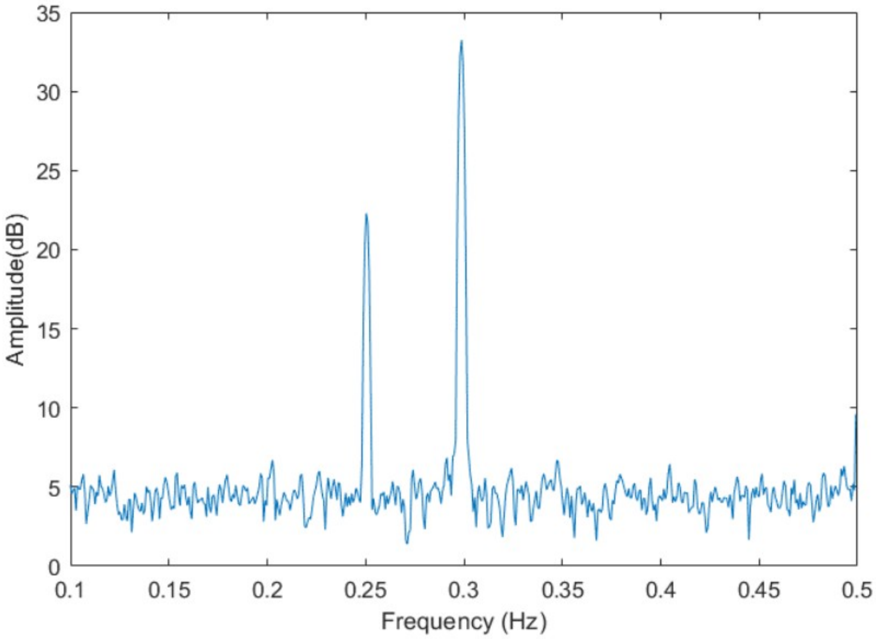

Figure 4.17: The spectrum of the sensor array output when two sensors are modulated with 250 Hz and 300 Hz respectively.

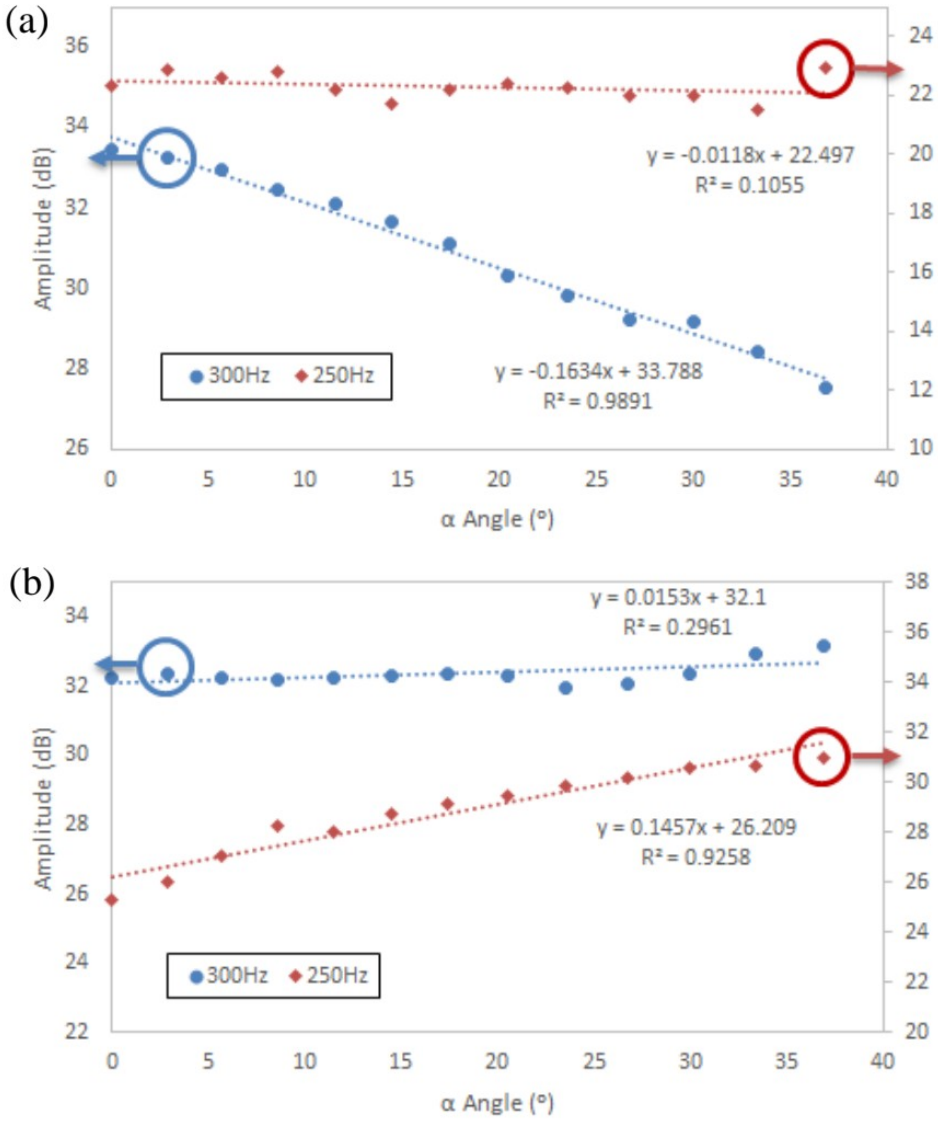

Figure 4.18: The twist measurement results when twisting (a) sensor 1 (300 Hz) and (b) sensor 2 (250 Hz).

4.3.5 Discussions

In this experiment, a conceptual optical device of tapered based sensor integrated with multiplexer was designed and demonstrated. The simultaneous twist sensing and sub-carrier multiplexing of LITF sensor was experimentally verified. The sensors were actively modulated with a specific sub-carrier frequency externally by using an acoustic source. When it was subjected to twist measurement, the sub-carrier modulated signal will be intensity modulated according to the twist angle. Therefore, multiple intensity modulated signals will be distinguishable on overlapping optical spectra by encoding each sensor with a specific sub-carrier frequency.

Signal-to-noise ratio of the pristine signal was 31.7 dB and the multiplexed signal in SCM sensing array was 25.9 dB. The attenuation due to the sub-carrier multiplexing system was less than 20%. Mapping of both pristine and multiplexed signals also showed a good agreement with an r^2 value of 0.9867.

Both sensors in the sensing array were subjected to twist measurement separately and achieved sensitivities of 0.1634 dB/° and 0.1457 dB/° respectively. The IMD occurred due to the sensing array was relatively small compared to the signal, which were 0.0118 dB/° and 0.0153 dB/° respectively. Although the effect of IMD was relatively small compared to the signal, it should be taken into consideration in future experiments when devising a more precise and accurate device.

CHAPTER 5

CONCLUSION AND FUTURE WORK

5.1 Conclusion

In the first part of this project, the implementation of MZI sensor on CFS roof truss was feasible and the repeatability sensing was proven. The results of MZI sensor showed a very high agreement with the conventional LVDT sensor on both trusses. In the cyclic load tests, the average percentage error of the repeatability sensing is ±5%. In the failure load test, the MZI sensor had achieved a sensitivity of 0.0032 μ/km^{-1} within the range of 1.880 km^{-1} to 3.324 km^{-1} and the deviation from conventional LVDT sensor is ±3%.

In the second part of the project, a simple, direct and effective way to operate multiple MZI sensors was demonstrated by using parallel topology. A real time monitoring of two MZI sensors was demonstrated, and the feasibility was verified. The attenuation of the signals in the SDM sensing array was very small. The regression coefficient, r^2 of mapping between pristine and multiplexed setups which is 0.9616 indicates that the results of MZI sensor in pristine and multiplexed setups are high in resemblance.

In the last part, a conceptual optical device of tapered based sensor integrated with multiplexer was designed and demonstrated. The simultaneous twist sensing and sub-carrier multiplexing of LITF sensor was experimentally verified. The sensors were actively modulated with a specific sub-carrier frequency externally by using an acoustic source. When the device was subjected to twist measurement, the sub-carrier modulated signal was further intensity modulated according to the twist angle. Therefore, the combined output signals were distinguishable on overlapping optical spectra by encoding each sensor with a specific sub-carrier frequency.

Signal-to-noise ratio of the pristine signal was 31.7dB and the multiplexed signal in SCM sensing array was 25.9dB. The attenuation due to the sub-carrier multiplexing system was less than 20%. Mapping of both pristine and multiplexed signals showed a good agreement r^2 value of 0.9867. In the demonstration of twist measurement, both LITF sensors achieved sensitivities of 0.1634 dB/° and 0.1457 dB/° respectively. The power shift of the static sensor shows the present of IMD when two sensor output were combined into one. Although the effect of IMD in this experiment was small enough to be neglected, but it has to be addressed when designing a mature optical sensing device.

5.2 Recommendations for Future Works

The feasibility of MZI sensor on lab-scale civil structures has been determined and the multiplexing solution to operate multiple MZI sensors has also been proven to be achievable. To further implement the MZI sensor in SHM, a more reliable and effective multiplexing system is needed to operate two or more number of MZI sensors to conduct multipoint sensing field test on a larger scale.

The reliability and the compactness of the LITF sensor has to be improved in order to be applied in the field test. One of the possible ways is to replace the commercial speaker unit with a smaller size piezoelectric transducer. However, the change in acoustic source might reduce the strength of the acoustic modulation signal. The coupling of the source to the sensor needs to be taken into consideration when designing the sensor. Another improvement is to design a packaging for LITF sensor to provide extra protection so that the sensor able to work in harsh measurement environments.

Another factor that might affect the sensor’s accuracy is the crosstalk effect which will occur when more than two LITF sensors are added into the sensing array. The characterization of the crosstalk effect is essential in amending the results in order to improve the accuracy of the optical sensor.

REFERENCES

Berthold, J. W. (1995). Historical Review of Microbend Fiber-Optic Sensors. Journal of Lightwave Technology, Vol. 13, No. 7, pp 1193.

Bohnert, K., Gabus, P., Kostovic, J., and Brandle, H., (2005). Optical fiber sensors for the electric power industry. Optics and Lasers in Engineering 43 (2005) 511-526.

Bucaro, J. A., Dardy, H. D., and Carome, E. F. (1977). Optical fiber acoustic fiber. U.S. Naval Research Laboratory, Washington, D.C. 20375.

Chan, D., Lin, H. S., and Phua, Y. N. (2020). Feasible study of fiber acoustic sensor by utilizing time domain reconstruction. 2020 IEEE Sensors Applications Symposium (SAS), pp. 1-5.

Cheng, R., and Xia, L. (2015) Wavelength interrogation of fiber Bragg grating sensors based on crossed optical Gaussian filters. Optics Letters, Vol. 40, No. 8, pp 1760-1763.

Senior, J. M., Moss, S. E., and Cusworth, S. D. (1990). Multiplexing Techniques for Non interferometric Optical Point-Sensor Networks: A Review. Fiber and Integrated Optics, 17:1, 3-20.

Deepa, S., Randhir, B., Asha, K., and Vinod, P. (2014). Intensity modulation using chirped fiber Bragg grating as an edge filter for temperature sensing. Microwave and optical technology letters, Vol. 56.

Doebling, S.W., Farrar, C.R., Prime, M.B., and Shevitz, D.W. Damage identification and health monitoring of structural and mechanical systems from changes in their vibration characteristics: A literature review. United States: N. p., 1996. Web. doi:10.2172/249299.

Dones, F., and Varshneya, D. (1994). An overview of Time Division Multiplexing sensor technology. Proc. SPIE Vol. 2295, Fly- by-Light.

Fahad, A. G. and Chauhdry, M. A. (2016). Sultan Mizan Zainal Abidin Stadium Roof Collapse, Kuala Terengganu, Malaysia (Lack of Safety Issues). EPH – International Journal of Mathematics and Statistic, Volume-2, Issue-10.

Fernandes, C. S., Giraldi, M. T. M. R., Sousa, M. J., Costa, J. C. W. A., Gouveia, C., Jorge, P., and Franco, M. A. R. (2016). Curvature and Vibration Sensing Based on Core Diameter Mismatch Structures. IEEE Transactions on Instrumentation and Measurement, Vol. 65, No. 9, pp 2120-2128.

Fidanboylu, K. A. and Efendioglu, H. S. (2009). Fiber Optic Sensors and Their Applications. 5th International Advanced Technologies Symposium (IATS'09), May 13-15, 2009, Karabuk, Turkey.

Fu, X., Zhang, J., Wang, S., Fu, G., Liu, Q., Jin, W., and Bi, W. (2016). A refractive index sensor based on taper Michelson interferometer in multimode fiber. Proceeding Volume 10025, Advanced Sensor Systems and Applications VII, 100251K, 2016.

Gan, J. C., Lim, J. H., Lim, S. K., and Lin, H. S. (2018). Experimental study on the effect of heel plate thickness on the structural integrity of cold-formed steel roof trusses. IOP Conference Series: Material Science and Engineering 431 (2018) 112009

Giraldi, M. T. M. R., Fernandes, C. S., Ferreira, M. S., Sousa, M. J. de, Jorge, P. A. S., Costa, J. C. W. A., Santos, J. L. C. O., and Frazao, O. (2015). Fiber loop mirror sensors interrogated and multiplexed by OTDR. Journal of Lightwave Technology, Vol. 33, No. 12, pp 2580-2584.

Guozhen, Y., Yongqian, L., and Zhi, Y. (2016). A novel fiber Bragg grating acceleration sensor for measurement of vibration. Optik, 127(20), 8874–8882.

Ibrahim, S. K., Roosbroeck, J. V., O'Dowd, J. A., and Hoe, B. V. (2016). Interrogation and mitigation of polarization effects for standard and birefringent FBGs. Proc. of SPIE, Vol. 9852 98520.

Inaudi, D., Vurpillot, S., Casanova, N., and Kronenberg, P. (1998). Structural monitoring by curvarure analysis using interferometric fiber optic sensors. Smart Mater. Struct. 7 (1998) 199-208.

Islam, M. R., Ali, M. M., Lai, M. H., Lim, K. S., and Ahmad, H. (2014). Chronology of Fabry-Perot Interferometer Fiber-Optic Sensors and Their Applications: A Review. Sensors 2014, 14, 7451-7488.

Jarzebinska, R., Chehura, E., James, S. W., and Tatam, R. P. (2012). Multiplexing a serial array of tapered optical fibre sensors using coherent optical frequency domain reflectometry. Meas. Sci. Technol. 23, 105203.

Jason, J. (2008). Theory and Applications of Coupling Based Intensity Modulated Fibre-Optic Sensors. (Licentiate dissertation). Mittuniversitetet, Sundsvall. Retrieved from http://urn.kb.se/resolve?urn=urn:nbn:se:miun:diva-7057

Ji, C., Zhao, C. L., Kang, J., Dong, X., and Jin, S. (2012). Multiplex and simultaneous measurement of displacement and temperature using tapered fiber and fiber Bragg grating. Review of Scientific Instruments 83, 053109, pp. 1-5.

Johny, J., Smith, T., Bhavsar, K., and Prabhu, R. (2017). Design of fibre based highly sensitive acoustic sensor for underwater applications. OCEANS 2017 – Aberdeen.

Jun, S. W., Lee, H. D., and Kim, C. S. (2015). Optical Phase-Shift Interrogation Method with a Single-Ended PM-PCF Sensor. IEEE Photonics Technology Letters, Vol. 27, No. 11, pp 1185-1188.

Kersey, A. D., Davis M. A., Patrick H. J., LeBlanc, M., Koo, K. P., Askins, C. G., Putnam, M. A., and Friebele, E. J. (1997). Fiber Grating Sensors. Journal of Lightwave Technology, Vol. 15, No. 8.

Kim, W., Lorenzo, T., and Jon, H. (2018). Bridges across Europe are in a dangerous state, warn experts. s.l.: The Guardian.

Korposh, S., James, S. W., Lee, S. W., and Tatam, R. P. (2019). Tapered Optical Fibre Sensors: Current Trends and Future Perspectives. Sensors 2019, 19(10), 2294.

Kreuzer, M. (2006). Strain measurement with fiber Bragg grating sensors. S2338-1.0 e, HBM GmbH, Darmstadt, Germany, 2006.

Krohn, D. A. (1988). Fiber Optic Sensors: Fundamental and Applications. Instrument Society of America, Research Triangle Park, North Carolina, 1988.

Lee, B. H., Kim,Y. H., Park, K. S., Eom, J. B., Kim, M. J., Rho, B. S., and Choi, H. Y. (2012). Interferometric Fiber Optic Sensors. Sensors 2012, vol. 12, pp. 2467-2486.

Li, B., Jiang, L., Wang, S., Zhou, L., Xiao, H., and Tsai, H. (2011). Ultra-Abrupt Tapered Fiber Mach-Zehnder Interferometer Sensors. Sensors 2011, 5729-5739.

Liang, X., Liu, Z., Wei, H., Li, Y., and Jian, S. (2015). Detection of liquid level with a MI based fiber laser sensor using few-mode EMCF. IEEE Photonics Technology Letters, Vol. 27, Issue 8, 15 April 2015.

Lim, J. H., Jang, H. S., and Lee, K. S. (2004). Mach-Zehnder interferometer formed in a photonic crystal fiber based on a pair of long-period fiber gratings. Optics Letters, Vol. 29, No. 4.

Lin, H. S., Mokhtar, M. R., Abdul Rashid, H. A., and Rahman, F. A. (2009). Simultaneous Sensing System for Identical Long-Period Gratings Sensors Using Subcarrier Multiplexing. Laser Physics, 2009, Vol. 19, No. 7, pp, 1-4.

Lin, H. S., Raji, Y. M., Lim, J. H. Lim, S. K., Mokhtar, M. R., and Yusoff, Z. (2016). Packaged in-line Mach-Zehnder interferometer for highly sensitive curvature and flexural strain sensing. *Sensors and Actuators A: Physical,* Vol. 250, p. 237-242.

Lopez-Higuera, J. M., Cobo, L. R., Incera, A. Q. and Cobo, A. (2011). Fiber Optic Sensors in Structural Health Monitoring. Journal of Lightwave Technology, Vol. 29, No. 4.

Lupi, C., Felli, F., Brotzu, A., Caponero, M. A., and Paolozzi, A. (2008). Improving FBG Sensor Sensitivity at Cryogenic Temperature by Metal Coating. IEEE Sensors Journal, 8(7), 1299–1304.

Markovic, M. Z., Bajic, J. S., Batilovic, M., Sušic, Z., Jožа, A., and Stojanovic, G. M. (2019). Comparative Analysis of Deformation Determination by Applying Fiber-optic 2D Deflection Sensors and Geodetic Measurements. Sensors 2019, Vol. 19, 844.

Majumder, M., Gangopadhyay, T. K., Chakraborty, A. K., Dasgupta K., and Bhattacharya, D. K. (2008). Fiber Bragg gratings in structural health monitoring – Present status and applications. Sensors and Actuatours A 147 (2008) 150-164.

Metje, N., Chapman, D. N., Rogers, C. D. F., Henderson, P., and Beth, M. (2008). An Optical Fiber Sensor System for Remote Displacement Monitoring of Structures - Prototype Tests in the Laboratory. Structural Health Monitoring: An International Journal, 7(1), 51–63.

Morey, W. W., Meltz, G. and Glenn, W. H. (1989). “Fiber Bragg grating sensors,” in Proc. SPIE Fiber Optic & Laser Sensors VII, 1989, vol. 1169, p. 98.

Mukhtar, W. M., Shaari, S. and Menon, P. S. (2010). Fabrication of optical fiber microprobe using electric arc heating and one-sided pulling technique. 2010 IEEE Student Conference on Research and Development (SCOReD).

Nathalie, M., Ayoub, C., Patrick, M., and Michel, C., (1995). Angular displacement fiber-optic sensor: theoretical and experimental study. Applied Optics, Vol. 34, No. 28.

Nurulain, S., Mazlee, N. N., Salim, M. R., and Manap, H. (2017). A review on optical fibre sensor topology and modulation technique. International Journal of Engineering Technology and Science (IJETS), Vol. 7.

Ong, K. S., Png, W. H., Lin, H. S., Pua, C. H., and Rahman, F. A. (2017). Acoustic Vibration Sensor Based on Macro-Bend Coated Fiber For Pipeline Leakage Detection. 2017 17th International Conference on Control, Automation and Systems (ICCAS), pp. 167-171.

Peng, P. C., Lim, J. H., Tseng, H. Y., and Chi, S. (2004). Intensity and wavelength division multiplexing FBG sensor system using a tunable multiport fiber ring laser. IEEE Photonics Technology Letters, Vol 16, No.1.

Png, W. H., Lin, H. S., Pua, C. H., Lim, J. H., Lim, S. K., Lee, Y. L. & Rahman, R. A. (2018). Feasibility use of in-line Mach–Zehnder interferometer optical fibre sensor in lightweight foamed concrete structural beam on curvature sensing and crack monitoring. *Structural Health Monitoring*. Volume 17(5), pp. 1277–1288.

Png, W. H., Lin, H. S., Pua, C. H., and Rahman, F. A. (2018). Pipeline monitoring and leak detection using Loop integrated Mach Zehnder Interferometer optical fiber sensor. Optical Fiber Technology, 46, 221–225.

Raji, Y. M., Lin, H. S., Ibrahim, S.A., Mokhtar, M. R., and Yusoff, Z. (2016). Intensity-modulated abrupt tapered fiber Mach-Zehnder Interferometer for the simultaneous sensing of temperature and curvature. Optics & Laser Technology 86 (2016) 8-13, 2016.

Rao, Y. J., Lobo-Ribeiro, A.B., Jackson, D. A., Zhang, L., and Bennion, I. (1996). Simultaneous spatial, time and wavelength division multiplexed in-fibre grating sensing network. Optics Communications 125(1996), pp. 53-58.

Rong, Q., Qiao, X., Wang, R., Sun, H, Hu, M. and Feng, Z. (2012). High-Sensitive Fiber-Optic Refractometer Based on a Core-Diameter-Mismatch Mach-Zehnder Interferometer. IEEE Sensors Journal, Vol. 12, No. 7, July 2012.

Rong, Q., Guo, T., Bao, W., Shao, Z., Peng, G.-D., and Qiao, X. (2017). Highly sensitive fiber-optic accelerometer by grating inscription in specific core dip fiber. Scientific Reports, 7(1).

Roslina, M., Mokhtar, M. R., Abdul Rashid, H. A., and Yusoff Z. (2018). Passive sub-carrier multiplexing for discriminating overlapped optical spectra. IEEE Photonics Technology Letters, Vol. 30, Issue 20, pp. 1784-1787.

Sikarwar, S., Satyendra, Singh, S., and Yadav, B. C. (2017). Review on pressure sensors for structural health monitoring. Photonic Sensors, 7(4), 294–304.

Soh, C. Y. (2018). Development of pipeline leak location detection based on leakage-induced acoustic waveform. Lee Kong Chian Faculty of Engineering and Science, Universiti Tunku Abdul Rahman, May 2018.

Sohn, H., Farrar, C. R., Hemez, F., & Czarnecki, J. (2002). *A Review of Structural Health Monitoring Literature 1996 – 2001*. Los Alamos National Laboratory Report, United States: N. p., 2002.

Takahashi, M., Noda, H., Terai, K., Ikuta, S., Mizutani, Y., Yokota, T., Kaminishi, T., and Tamagawa, T. (1997). Optical Current Transformer for Gas Insulated Switched Using Silica Optical Fiber. IEEE Transactions on Power Delivery, Vol. 12, No. 4.

Tian, Z., Yam, S. S., and Loock, H. P. (2008). Refractive index sensor based on an abrupt taper Michelson interferometer in a single-mode-fiber. Optics Letters, Vol.33, No. 10.

Wallis, S. (2012). Tunnel ceiling collapse kills in Japan. s.l.: TunnelTalk.

Wang, Y., Yang, M., Wang, D. N., Liu, S., and Lu, P. (2010). Fiber In-line Mach-Zehnder Interferometer Fabricated by Femtosecond Laser Micromachining for Refractive Index Measurement with High Sensitivity. J. Opt. Soc. Am. B/Vol. 27.

Wang, Y., Yuan, H., Liu, X., Bai, Q., Zhang, H., Gao, Y., and Jin, B. (2019). A comprehensive study of optical fiber acoustic sensing. IEEE Access, Vol. 7, pp 85821 – 85837.

Ward, J. M., O'Shea, D.G., Shortt, B. J., Morrissey, M. J., Deasy, K., and Chormaic, S. G (2006). A heat-and-pull rig for fiber taper fabrication. Review of Scientific Instruments 77, 083105 (2006).

Wild G., and Hinckley, S. (2008). Acousto-ultrasonic optical fiber sensors: overview and state-of-the-art. IEEE Sens. J. 8, pp. 1184–1193.

Xu, B., Li, Y., Sun, M., Zhang, Z. W., Dong, X. Y., Zhang, Z. X., and Jin, S. Z. (2012). Acoustic vibration sensor based on nonadiabatic tapered fibers. Optics letters, Vol. 37, No. 22, pp. 4768-4770.

Yao, Q., Meng, H., Wang, W., Xue, H., Xiong, R., Huang, B., Tan, C., and Huang, X. (2014). Simultaneous measurement of refractive index and temperature based on a core-offset Mach-Zehnder interferometer combined with a fiber Bragg grating. Sensors and Actuators A: Physical, Vol, 209, pp. 73-77.

Yuan, D., Dong, Y., Liu, Y., and Li, T. (2015). Mach-Zehnder interferometer biochemical sensor based on silicon-on-insulator rib waveguide with large cross section. Sensors 2015, 15, 21500-21517.

Zhang, Y., Su, H., Ma, K., Zhu, F., Guo, Y., and Jiang, W. (2018). Optic-fiber temperature sensor. Intech Open, 25th July 2018. Available at: https://www.intechopen.com/books/temperature-sensing/optic-fiber-temperature-sensor.

Zhou, J., Wang, Y., Liao, C., Sun, B., He, J., Yin, G., Liu, S., Li, Z., Wang, G., Zhong, X., and Zhao. J. (2014). Intensity modulated refractive index sensor based on optical fiber Michelson interferometer. Sensors and Actuators B 208, pp. 315-319.

Zhu, Z., Liu, L., Liu, Z., Zhang, Y., and Zhang, Y. (2017). High-precision micro-displacement optical-fiber sensor based on surface plasmon resonance. Optics Letters, 42(10), 1982.

LIST OF PUBLICATIONS

Oon, W. L., Lin, H. S., Pua, C. H., Lim, J. H., Lim, S. K., Ong, C. F., and Rahman, F. A. Simultaneous sensing of Mach-Zehnder interferometer optical sensor arrays using spatial division multiplexing. 2018 IEEE Student Conference on Research and Development (SCOReD), pp. 1-4.

Oon, W. L., Lin, H. S., Pua, C. H., Lim, J. H., Lim, S. K., and Rahman, F. A. (2019). Feasibility of packaged interferometric photonics micro-taper sensor for cold-formed steel roof truss structural health monitoring. 2019 IEEE 9th International Nanoelectronics Conferences (INEC), pp. 1-4.